JOURNAL OF GEOPHYSICAL RESEARCH, VOL. 109, D23S11, doi:10.1029/2004JD004513, 2004

Multiscale simulations of tropospheric chemistry in the eastern Pacific and on the U.S. West Coast during spring 2002

Youhua Tang,[1] Gregory R. Carmichael,[1] Larry W. Horowitz,[2] Itsushi Uno,[3] Jung-Hun Woo,[1] David G. Streets,[4] Donald Dabdub,[5] Gakuji Kurata,[6] Adrian Sandu,[7] James Allan,[8] Elliot Atlas,[9] Franck Flocke,[9] Lewis Gregory Huey,[10] Roger O. Jakoubek,[11] Dylan B. Millet,[12] Patricia K. Quinn,[13] James M. Roberts,[11] Douglas R. Worsnop,[14] Allen Goldstein,[12] Stephen Donnelly,[9] Sue Schauffler,[9] Verity Stroud,[9] Kristen Johnson,[9] Melody A. Avery,[15] Hanwant B. Singh,[16] and Eric C. Apel[9]

Received 5 January 2004; accepted 10 March 2004; published 9 July 2004.

[1] Regional modeling analysis for the Intercontinental Transport and Chemical Transformation 2002 (ITCT 2K2) experiment over the eastern Pacific and U.S. West Coast is performed using a multiscale modeling system, including the regional tracer model Chemical Weather Forecasting System (CFORS), the Sulfur Transport and Emissions Model 2003 (STEM-2K3) regional chemical transport model, and an off-line coupling with the Model of Ozone and Related Chemical Tracers (MOZART) global chemical transport model. CO regional tracers calculated online in the CFORS model are used to identify aircraft measurement periods with Asian influences. Asian-influenced air masses measured by the National Oceanic and Atmospheric Administration (NOAA) WP-3 aircraft in this experiment are found to have lower ΔAcetone/ΔCO, ΔMethanol/ΔCO, and ΔPropane/ΔEthyne ratios than air masses influenced by U.S. emissions, reflecting differences in regional emission signals. The Asian air masses in the eastern Pacific are found to usually be well aged (>5 days), to be highly diffused, and to have low NO_y levels. Chemical budget analysis is performed for two flights, and the O_3 net chemical budgets are found to be negative (net destructive) in the places dominated by Asian influences or clear sites and positive in polluted American air masses. During the trans-Pacific transport, part of gaseous HNO_3 was converted to nitrate particle, and this conversion was attributed to NO_y decline. Without the aerosol consideration, the model tends to overestimate HNO_3 background concentration along the coast region. At the measurement site of Trinidad Head, northern California, high-concentration pollutants are usually associated with calm wind scenarios, implying that the accumulation of local pollutants leads to the high concentration. Seasonal variations are also discussed from April to May for this site. A high-resolution nesting simulation with 12-km horizontal resolution is used to study the WP-3 flight over Los Angeles and surrounding areas. This nested simulation significantly improved the predictions for emitted and secondary generated species. The difference of photochemical behavior between the coarse (60-km) and nesting simulations is discussed and compared with the observation. *INDEX TERMS:* 0317 Atmospheric Composition and Structure: Chemical kinetic and photochemical properties; 0365 Atmospheric Composition and Structure: Troposphere—composition and chemistry; 0368 Atmospheric

---

[1] Center for Global and Regional Environmental Research, University of Iowa, Iowa City, Iowa, USA.

[2] Geophysical Fluid Dynamics Laboratory, NOAA, Princeton, New Jersey, USA.

[3] Research Institute for Applied Mechanics, Kyushu University, Fukuoka, Japan.

[4] Decision and Information Sciences Division, Argonne National Laboratory, Argonne, Illinois, USA.

[5] Department of Mechanical and Aerospace Engineering, University of California, Irvine, California, USA.

[6] Department of Ecological Engineering, Toyohashi University of Technology, Toyohashi, Japan.

0148-0227/04/2004JD004513$09.00

[7] Department of Computer Science, Virginia Polytechnic Institute and State University, Blacksburg, Virginia, USA.

[8] Department of Physics, University of Manchester Institute of Science and Technology, Manchester, UK.

[9] National Center for Atmospheric Research, Boulder, Colorado, USA.

[10] School of Earth and Atmospheric Sciences, Georgia Institute of Technology, Atlanta, Georgia, USA.

[11] Aeronomy Laboratory, NOAA, Boulder, Colorado, USA.

[12] Department of Environmental Science, Policy, and Management, University of California, Berkeley, California, USA.

[13] Pacific Marine Environmental Laboratory, NOAA, Seattle, Washington, USA.

[14] Aerodyne Research Inc., Billerica, Massachusetts, USA.

[15] NASA Langley Research Center, Hampton, Virginia, USA.

[16] NASA Ames Research Center, Moffett Field, California, USA.

Composition and Structure: Troposphere—constituent transport and chemistry; 3337 Meteorology and Atmospheric Dynamics: Numerical modeling and data assimilation; *KEYWORDS:* chemical transport model, nesting simulation, atmospheric photochemistry

Citation: Tang, Y., et al. (2004), Multiscale simulations of tropospheric chemistry in the eastern Pacific and on the U.S. West Coast during spring 2002, *J. Geophys. Res.*, *109*, D23S11, doi:10.1029/2004JD004513.

1. Introduction

[2] During April and May 2002 the Intercontinental Transport and Chemical Transformation 2002 (ITCT 2K2) experiment studied the air mass characteristics over the eastern Pacific and the U.S. West Coast. National Oceanic and Atmospheric Administration (NOAA) WP-3 aircraft and surface measurements were performed with the objective of characterizing the Asian inflow signal and its impact on regional air quality. During this period, air masses impacted by Asian emissions are transported to the eastern Pacific by the midlatitude prevailing westerlies. The long-distance transport of Asian pollutants to the west coast of North America has been studied by many researchers, such as *Jaffe et al.* [1999] and *Kotchenruther et al.* [2001]. *Jacob et al.* [1999] discussed the impact of Asian emissions variation on North America air quality using a global model. The strength of the Asian influence on North America was shown to depend on the Asian emission strength and the transport efficiency over the Pacific Ocean. Asian emissions are composed of anthropogenic (including biofuel) sources, biomass burning, and volcanic activity. *Woo et al.* [2003] estimated the biomass-burning emission during the spring 2001. *Carmichael et al.* [2003a, 2003b] studied the features of Asian outflow over the west Pacific and used aircraft measurements and model results to evaluate the emission estimations by *Streets et al.* [2003a, 2003b]. *Yienger et al.* [2000] described the Asian pollutant transport to North America using CO as the criteria. The trans-Pacific transport of aerosol is also an important issue. During springtime Asian dust storms become active, and dust can be transport to the eastern Pacific and North America [*Uno et al.*, 2001; *VanCuren and Cahill*, 2002]. However, during the ITCT 2K2 experiment the influence of Asian dust on North American was not significant.

[3] To study the transport and chemistry of trace gases and aerosols across the northern Pacific, we used a regional chemical transport model. Regional models have an advantage over global models in their ability to use finer resolutions in the analysis, but have the disadvantage of requiring lateral boundary conditions. In this study the lateral boundary conditions were established using a multiscale modeling system with nested models. Nesting techniques can help in the analysis from two sides: introducing external influences for relatively long-lived transported species, such as CO or O_3 [*Langmann et al.*, 2003], and by considering high-resolution emissions for short-lived species, such as NO_x or SO_2 [*Tang*, 2002]. High-resolution emissions can more accurately resolve near-source concentrations, and better estimate photochemical budgets [*Tang*, 2002].

[4] In this paper, the multiscale model is used to help analyze aircraft and surface measurements obtained during the ITCT 2K2 experiment. In the following section the details of the model are presented. In section 3 Asian tracer information calculated by the model is used to classify the aircraft observations into those observations with large and small Asian signals, which are then subsequently used to help quantify observed characteristics of Asian air masses over the eastern Pacific. Specific characteristics of individual aircraft flights are analyzed in section 4, where the multiscale model system is used to study the photochemistry in air masses over the eastern Pacific as aged air masses interact with emissions from North America. The WP-3 flight on 13 May over Los Angeles is analyzed as an example of the effect of model resolution on model predictions. The effect of aerosols on nitrate partitioning is presented in section 5. Results from a fine-scale nesting simulation of the flight around Los Angeles are presented in section 6. A mission-wide perspective of the performance of the model comprises section 7. Analysis of the Trinidad Head observations is presented in section 8.

2. Model System

[5] Characterizing the Asian influence on the chemistry of the eastern Pacific is a challenge as trace species are diluted during their trans-Pacific transport, which makes it difficult to distinguish them from background conditions. These air masses also mix with local sources as they move inland. To efficiently consider these processes, a multiscale model system was established. This model system includes the Model of Ozone and Related Chemical Tracers (MOZART) global chemical transport model [*Horowitz et al.*, 2003], the intercontinental chemical tracer model Chemical Weather Forecasting System (CFORS) [*Uno et al.*, 2003], and a nested regional chemical transport model, Sulfur Transport and Emissions Model 2003 (STEM-2K3) [*Tang et al.*, 2004]. The model domains are shown in Figure 1.

[6] CFORS is an online tracer model [*Uno et al.*, 2003] coupled with the RAMS regional meteorological model. In this application, CFORS was driven by NCEP reanalysis for postanalysis and AVN data for forecasting uses. CFORS treats chemical species as tracers assuming linear consumption. For example, NO_x tracer in CFORS decays with a first-order rate:

$$\frac{d[\mathrm{NO}_x]}{dt} = -k_{\mathrm{NO}x}[\mathrm{NO}_x], \tag{1}$$

where $k_{\mathrm{NO}x}$ is a fixed value. In CFORS, we define a conservative NO_y (total odd nitrogen species) tracer that can be transported without loss, and assume that this NO_y tracer has the same emission source as NO_x. Under this assumption, the NO_x age can be derived from equation (1):

$$T_{\mathrm{NO}x} = k_{nox}\ln\left([\mathrm{NO}_y]/[\mathrm{NO}_x]\right). \tag{2}$$

This equation allows for the online calculation of the averaged NO_x age when air masses from different sources

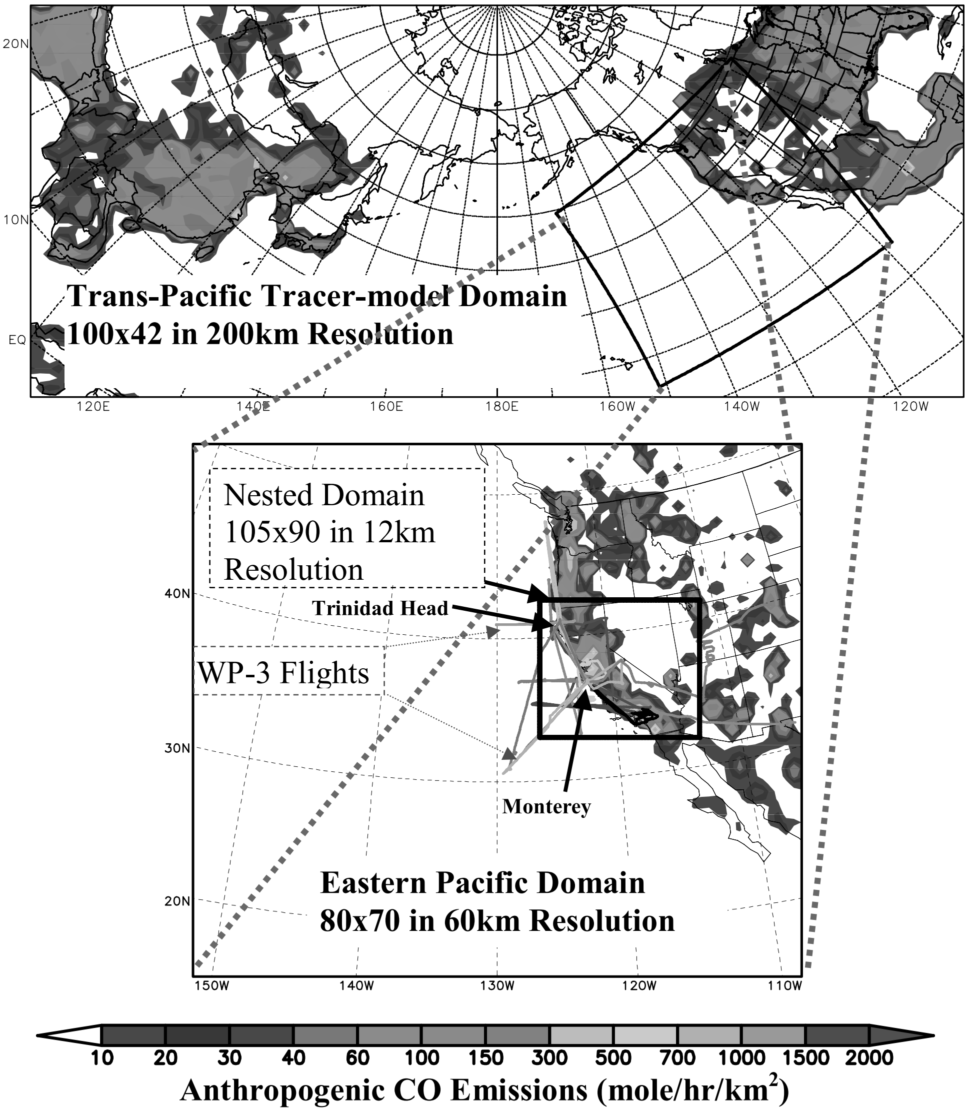

Figure 1. Model domains, NOAA WP-3 flight paths (colored lines), and estimated CO emissions on the various domains. See color version of this figure at back of this issue.

mix together. This NO_x age represents a combined result of transport time, diffusion, and NO_x source intensities. With the same method we also define a volatile organic compound (VOC) age using ethane as an indicator that is related to ethane emission and decay rate. In this study, the decay rates used in CFORS for CO, SO_2, NO_x and ethane were 2.22×10^{-7}, 2.78×10^{-6}, 9.26×10^{-6}, and 1.25×10^{-7} s^{-1}, respectively.

[7] CO is one of the primary tracers in CFORS and is used to help classify emission source types and regions. In this study CO was parsed into: Asian anthropogenic, biomass burning (BB), Mexico, Canada, California, Washington-Oregon, and the rest of the United States. These regional CO tracers can be used to help determine the air mass properties and its mixing state. During the ITCT 2K2 field campaign, forecast products for these tracers were also used for flight planning. It is important to note that these CO tracers in CFORS do not yield a total CO value that can be quantitatively compared to observed values because they represent primary CO only. The CFORS analysis does not consider CO that arises from methane and nonmethane hydrocarbon oxidation. Furthermore, the background levels were set to zero. In this paper, CFORS tracer model for ITCT 2K2 used a domain with 100 × 42 grids with a 200-km horizontal resolution (Figure 1), which covers east Asia, the northern Pacific Ocean, and most of North America.

[8] Comprehensive chemistry and transport interactions are calculated by the STEM-2K3 regional chemical transport model, which is a further development of the STEM-2K1 model [*Tang et al.*, 2003a; *Carmichael et al.*, 2003a] that includes the SAPRC-99 gaseous mechanism [*Carter*, 2000] and an explicit photolysis rate solver (the online NCAR Tropospheric Ultraviolet-Visible (TUV) radiation model, *Madronich and Flocke* [1999]). The main improvement of STEM-2K3 over STEM-2K1 is that the former also includes an aerosol thermodynamics module, Simulating Composition of Atmospheric Particles at Equilibrium (SCAPE II) [*Kim et al.*, 1993a, 1993b; *Kim and Seinfeld*, 1995], for calculating gas-particle equilibrium concentrations among inorganic aerosol ions and their gaseous

Table 1. The 17 Vertical Layers (Over the Sea Surface) Used in CFORS and STEM-2K3 and CO Background Profile in the Eastern Pacific

	Vertical Layers																
	1	2	3	4	5	6	7	8	9	10	11	12	13	14	15	16	17
Altitude, km	0.075	0.24	0.44	0.68	0.96	1.3	1.7	2.2	2.8	3.5	4.4	5.4	6.6	8.1	9.8	11.6	13.4
CO, ppbv	120	120	120	120	120	120	120	110	110	110	110	108	105	105	98	85	80

precursors. *Tang et al.* [2004] described the framework of STEM-2K3 and its performance during the Transport and Chemical Evolution over the Pacific (TRACE-P) experiment [*Jacob et al.*, 2003] and Asian Pacific Regional Aerosol Characterization Experiment (ACE-Asia). In this paper, the analysis includes inorganic aerosols in 4 size bins (in diameter): 0.1–0.3 μm, 0.3–1.0 μm, 1.0–2.5 μm, and 2.5–10 μm (referred to as bins 1–4, respectively). Daily Total Ozone Mapping Spectrometer (TOMS) data were used to calculate the model's overtop ozone column needed in the photolysis calculations using the TUV module.

[9] The primary domain for STEM-2K3 covers the U.S. West Coast and eastern Pacific with a 60-km horizontal resolution (Figure 1). Another RAMS model run in this domain was used to drive STEM-2K3. To better reflect the influence of more local sources, such as during the flight over the Los Angeles basin, a higher resolution is necessary. Here a nested domain with a nesting ratio of 1:5 (Figure 1) was used. The nested STEM-2K3 was driven by meteorology interpolated from the RAMS 60-km predication. The change in resolution affects the emission intensity. For example, Figure 1 shows that CO emission rate in Los Angeles ranges from 150 to 300 mole/h/km^2 represented in the domain of 200-km resolution, is over 1500 mole/h/km^2 in the 60-km domain, and greater than 3000 mole/h/km^2 (peak value) with 12-km resolution. *Tang* [2002] discussed how model resolution affected O_3 and NO_x predications, and photochemical correlations through for the TRACE-P and ACE-Asia experiments.

2.1. Lateral Boundary Conditions

[10] The MOZART global model was used to provide lateral boundary conditions for the STEM-2K3 primary 60-km domain (Figure 1) applications. The lateral boundary and top boundary conditions of STEM-2K3 for all species except CO were interpolated to the primary 60-km domain from the MOZART model results produced using NCEP winds. Because of the uncertainties in the CO emission inventories the global model tends to quantitatively underestimate CO in the midlatitudes and altitudes. The ITCT 2K2 aircraft observations showed that CO had a stable background concentration over the eastern Pacific, and CO contributions from various sources were mostly represented by enhancements above background. In this paper, we set the boundary condition of STEM-2K3 for CO to the background CO (shown in Table 1) plus a perturbation calculated as the total tracer CO from the CFORS model. The boundary values above the flight altitude of the WP-3 were obtained using the observations by the NASA DC-8 aircraft during the TRACE-P experiment. Table 1 also shows the model vertical layers used in CFORS and STEM-2K3, defined in the midpoint of the RAMS sigma-*z* layers [*Pielke et al.*, 1992]. The nested 12-km domain has the same vertical layers as the 60-km primary domain, and the lateral boundary conditions were also interpolated from the 60-km domain.

2.2. Emissions

[11] Emission data used in this study came from various sources. The basic strategy to develop the assembled emissions inventory was to use global-scale emissions inventories as background/lower quality assurance information, and to supplement these with more comprehensive/higher-quality regional-scale emissions data for Asia and North America regions. The Asian anthropogenic emissions were based on the estimate of *Streets et al.* [2003a, 2003b]. Biomass-burning emissions for Southeast Asia were based on April-averaged Asian BB emissions for the base year of 2001 [*Woo et al.*, 2003]. Emissions in the United State and Canada were based on the USEPA 1996 inventory. Mexican emissions came from *Kuhns et al.* [2001]. The ship emissions for CO, SO_2 and NO_x were based on the inventory of *Corbett et al.* [1999], and aviation emissions were taken from EDGAR [*Olivier et al.*, 1996]. Lightning NO_x emissions were diagnosed from the meteorological model according to deep convective intensities [*Pickering et al.*, 1998]. Emissions for all other regions in the 200-km domain came from Global Emissions Inventory Activities (GEIA) inventory http://geiacenter.org/). Biogenic emissions for the regions other than the United States come from GEIA [*Guenther et al.*, 1995]. MOZART global model has it own emission [*Horowitz et al.*, 2003], which is mainly based on the EDGAR inventory [*Olivier et al.*, 1996].

[12] For simulating pollutant recirculation from the western U.S. into the Pacific Ocean and propagation from the West Coast inland, we used U.S. EPA emission databases and more detailed allocation procedures. For example, the emission data for the nested 12-km domain (Figure 1) require a resolution higher than county scale. The original county-scale emissions were redistributed to the finer resolution grid system using high-resolution population data to give "within county" spatial variability. Further detail into the methodology for this approach used to generate high-resolution emissions for nested simulations can be found in the references elsewhere [*Woo et al.*, 2003; *Tang*, 2002].

3. Air Mass Characteristics

[13] The NOAA WP-3 aircraft performed 13 flights, including transit flights to and from the base in Monterey, California (Figure 1). One objective of these flights was to characterize Asian air masses over the eastern Pacific and how they are modified as they move over the American continent and mix with local sources. Identification of air masses impacted by Asian emissions is difficult because of the long transport times and the variety of sources impacting the Pacific Basin. Techniques for identifying Asian emission signals that rely on observation-based filters are

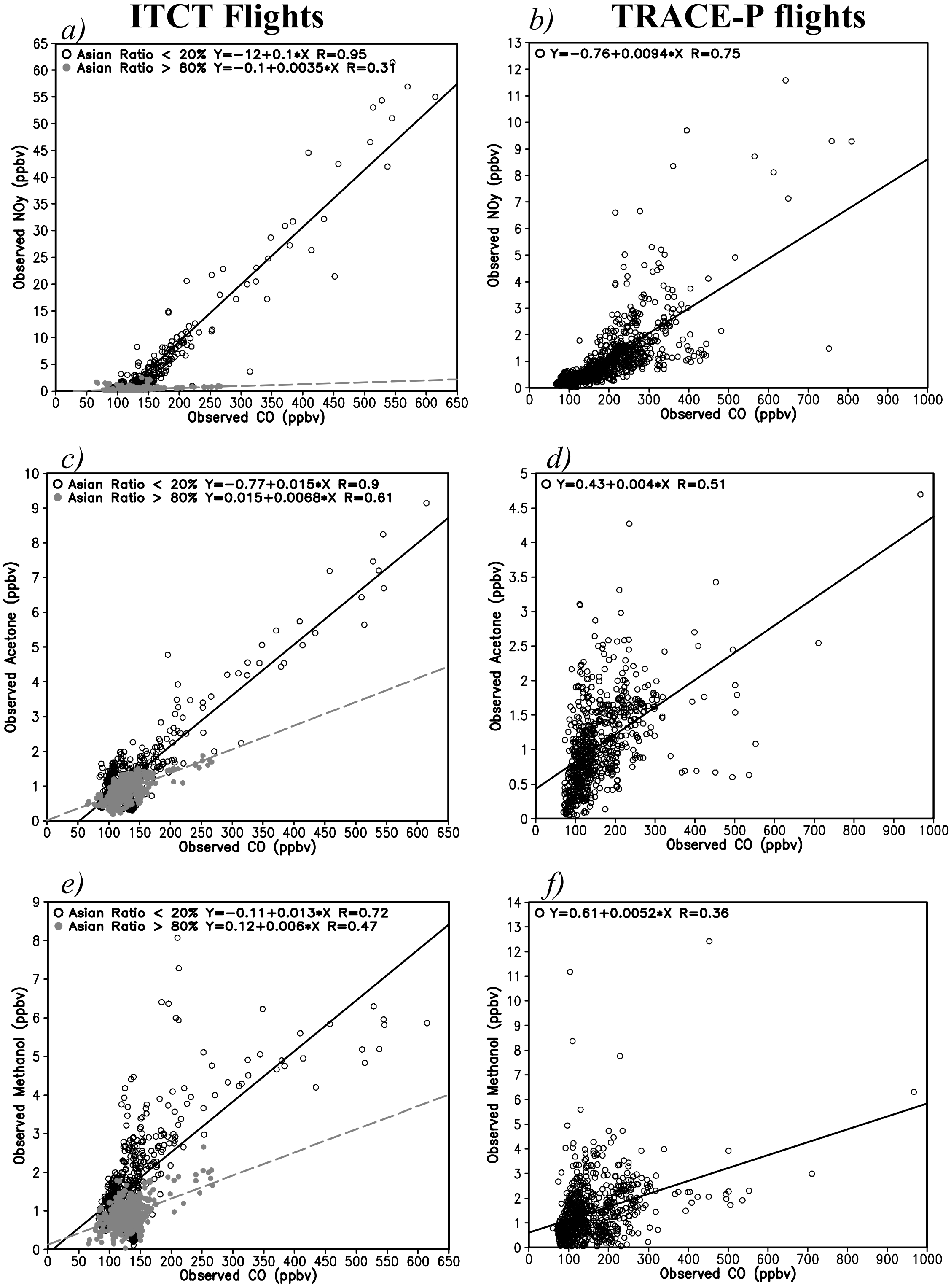

Figure 2. (a–j) ITCT aircraft-observed correlations (left panels) classified by simulated Asian ratios <20% and >80% and TRACE-P aircraft-measured correlations (right panels). All plots are marked with linear fit lines and correlation coefficient *R*.

discussed by *Nowak et al.* [2004] and *de Gouw et al.* [2004]. Alternatively, the model can be used to identify those air masses expected to contain Asian signals. We used an Asian air mass ratio, defined as the Asian anthropogenic CO tracer concentration divided by total anthropogenic tracer CO concentration in this domain, to identify air masses impacted by Asian sources. This metric was calculated for each WP-3 three-minute flight segment, and the aircraft data were then sorted using the model calculated Asian ratios. Figure 2 shows correlations of

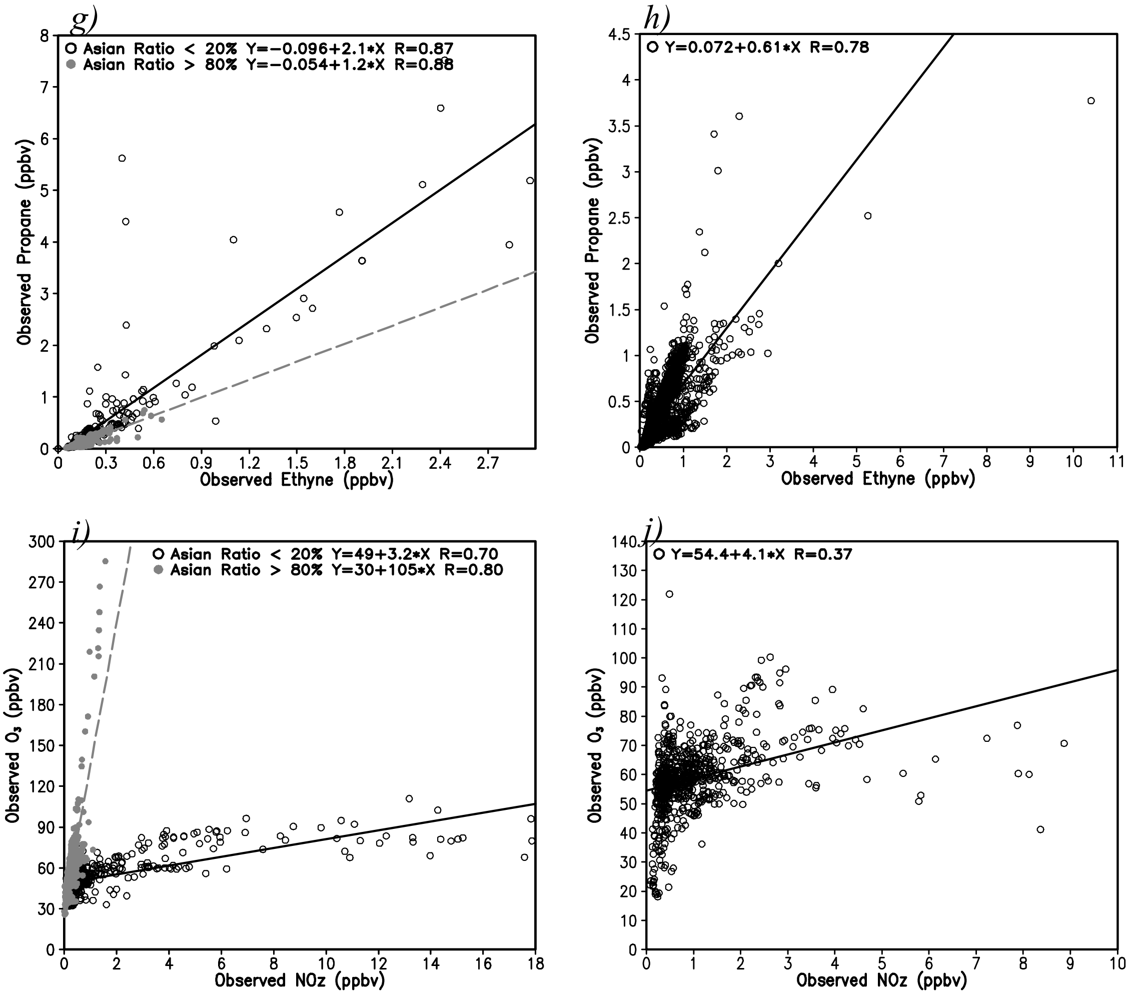

Figure 2. (continued)

observed species for air masses with Asian ratios <20% and those with values >80% using the 3-min merged data set for all ITCT WP-3 flights. The data points with Asian ratio <20% and >80% account for about 23% and 53% respectively in all WP-3 flights. Figure 2 also shows the air mass correlations of the observations taken on board the NASA DC-8 and P-3B aircrafts over the western Pacific during the TRACE-P experiment, March of 2001. Figures 2a and 2b show that Asian air masses have lower $\Delta NO_y/\Delta CO$ values in both the western Pacific and eastern Pacific than air masses dominated by American emissions. *Tang et al.* [2003b] found that BB plumes from Southeast Asia have low $\Delta NO_y/\Delta CO$ ratios (about 0.005 ppbv/ppbv). Asian air masses impacted by biofuel sources exhibit similar low ratios. The portion of emissions from gasoline in Asia is generally smaller than that in the United States [*Streets et al.*, 2003a]. For example, coal is the main fossil fuel used in China, and coal combustion also emits a lower $\Delta NO_y/\Delta CO$ than gasoline combustion. All these factors contribute to Asian air masses having a ~10 times lower $\Delta NO_y/\Delta CO$ ratio than American air masses. After long-distance transport the ratio in the Asian air masses decreases to ~0.0035 ppbv/ppbv (Figure 2a) because of NO_y's gas-particle conversion, and wet and dry depositions. This is discussed further in section 5.

[14] The air masses dominated by American sources show higher correlation coefficients than Asian air masses for CO versus acetone and methanol (Figures 2c–2f). These results imply that CO, acetone and methanol in the United States come from similar emission sources. Air masses with Asian ratios <20% have higher ΔAcetone/ΔCO and ΔMethanol/ΔCO ratios, reflecting the large petroleum refining and usage in the western United States.

[15] The lifetimes of propane and ethyne range from several days to several weeks. However, they have similar reaction rate with OH, the main reaction for their consumption. Figures 2g and 2h show that the ΔPropane/ΔEthyne ratio associated with Asian sources (1.2 ppbv/ppbv) is 70% lower than in American air masses, but still higher than the TRACE-P measurement since Asian air masses in the eastern Pacific are mixed with North American sources.

[16] The values presented above based on a model-based screening for Asian plumes can be compared to values calculated on the basis of observation-based plume identification. An observation-based Asian plumes value of $\Delta NO_y/\Delta CO$ for the 5 May flight for altitudes >5 km of 0.003 ppbv/ppbv was reported by *de Gouw et al.* [2004], while values of 0.0035–0.0049 ppbv/ppbv for all identified Asian plumes were calculated by *Nowak et al.* [2004]. In terms of ΔPropane/Δethyne, observed values ranged from

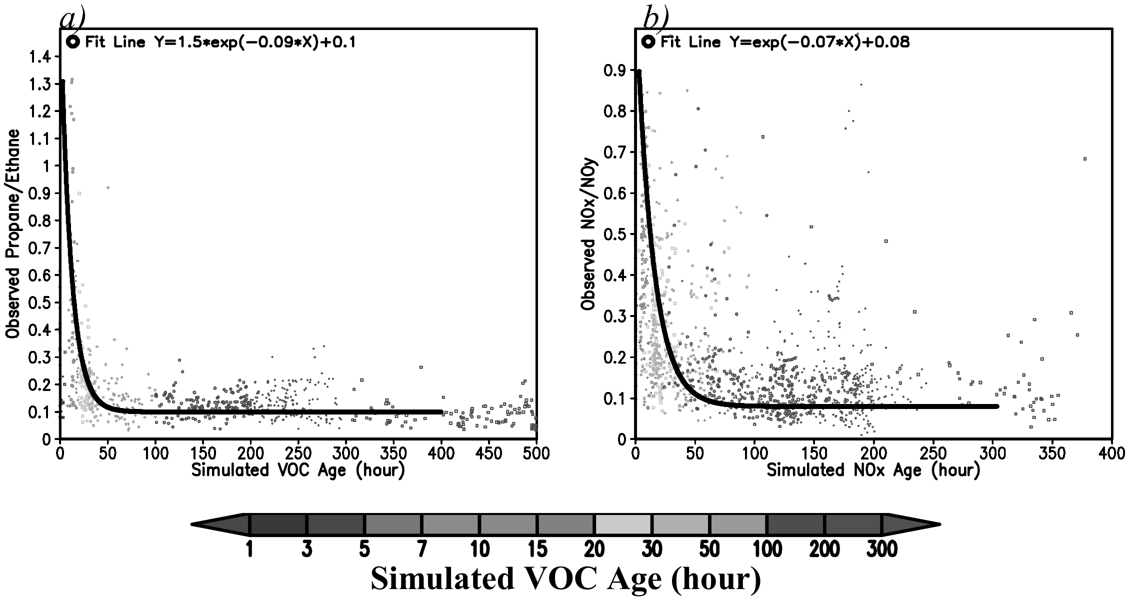

Figure 3. (a and b) Observed ratios versus VOC age and NO_x age estimated by the CFORS model for all ITCT flights, color-coded by VOC age. See color version of this figure at back of this issue.

1.5 to 1.1 ppbv/ppbv for the 5 May and 17 May flights, respectively, which represent the two most heavily influenced Asian events. These results indicate that the model-based approach provides a consistent and four-dimensional contextual method to help identify Asian air masses.

[17] The observations also provide indicators of ozone production. NO_z (NO_y-NO_x) represents the oxidized products of NO_x, including peroxyacetyl nitrate (PAN), HNO_3, HNO_2, etc. The ratio $\Delta O_3/\Delta NO_z$ represents the upper limit of the ozone production efficiency (OPE) per unit NO_x [*Trainer et al.*, 1993]. Figure 2i shows this ratio for the air masses with Asian ratios <20% and >80%, and O_3 and NO_z have relatively strong correlations in both sets of data. The $\Delta O_3/\Delta NO_z$ ratio in Asian air masses over the eastern Pacific is higher than that in American air masses and in air masses over the western Pacific (Figure 2j). The very high $\Delta O_3/\Delta NO_z$ of Asian air masses over the eastern Pacific (Figure 2i) is not solely due to the accumulation of NO_x photochemically generating O_3. The NO_z conversion to nitrate aerosol and depositions also results in an increase in this ratio. This was shown to be important in the Asian outflow during ACE-Asia, and where most of the nitrate was concentrated in the supermicron particles, and thus were more rapidly removed from the air via deposition processes [*Tang et al.*, 2004].

[18] Classification of the air mass age is an important element of analysis. Air mass age can be estimated from trajectory analysis [*Cooper et al.*, 2004]. This can also be done using observed chemical ratios as discussed by *de Gouw et al.* [2004]. The multiscale model also includes indicators of chemical age. Figure 3 shows the observed Propane/Ethane and NO_x/NO_y ratios plotted against predicted CFORS VOC and NO_x ages, respectively. The aircraft measurements indicate that fresh air masses from the United States have Propane/Ethane ratios >1, but air masses with ages >50 hours have ratios <0.4. The main consumption of propane and ethane in the atmosphere is through reactions with OH, and the reaction constant for propane is about four times bigger than that for ethane. Figure 3a shows that the Propane/Ethane ratio declines very fast within the first 50 hours. After 50 hours this ratio takes values between 0.02 and 0.3. The relation between observed NO_x/NO_y and predicted NO_x age (Figure 3b) is similar to that between Propane/Ethane and VOC age. The best fit lines in Figure 3 show the lower limits to be 0.1 for Propane/Ethane and 0.08 for NO_x/NO_y.

[19] The points in Figures 3a and 3b are color-coded using CFORS VOC age. The results for the NO_x age show that the two age metrics produce consistent results. The fraction of NO_x in NO_y shows more variability at a given age than the Propane/Ethane ratio, which reflects the complexity of the NO_x chemistry relative to that for propane and ethane. In fresh polluted air masses NO_x usually is converted to NO_z through photochemical reactions, and O_3 is one of the by-products during this conversion. However, some reactions, such as the photolysis of PAN, recycle NO_z back to NO_x. The ITCT measurements indicate that some NO_y enhancements at high altitudes were associated with stratospheric intrusions, implying that stratospheric contribution to NO_y or NO_x via N_2O dissociation [*Strahan*, 1999] could be significant for these flights.

4. Case Studies

[20] The multiscale modeling system was used in forecast mode for flight planning and in postanalysis mode to help interpret the observations. The air mass age discussion in the previous section indicated that the air masses from Asia took on the order of one week to reach the eastern Pacific. During this transport journey, dynamic mixing and dispersion processes act to decrease the air mass concentrations. This fact, coupled with the complexity of the interactions between aged air masses and fresh emissions from the western United States, make it difficult to interpret the

a) Simulated Anthropogenic CO and Its Asian Ratio in the 1 km layer

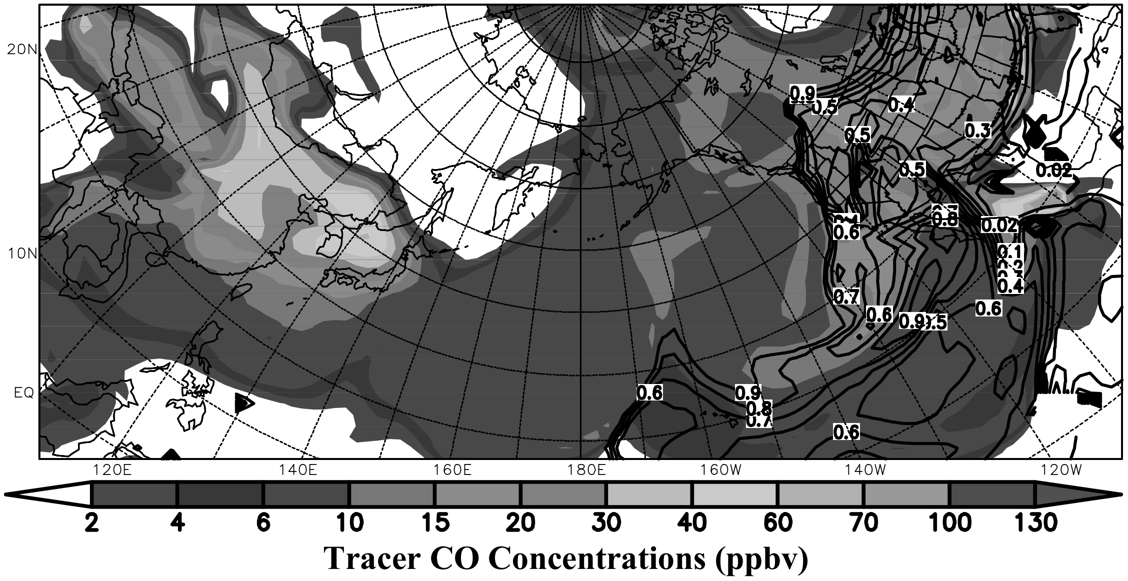

b) Simulated Anthropogenic CO and Its Asian Ratio in the 5.4 km layer

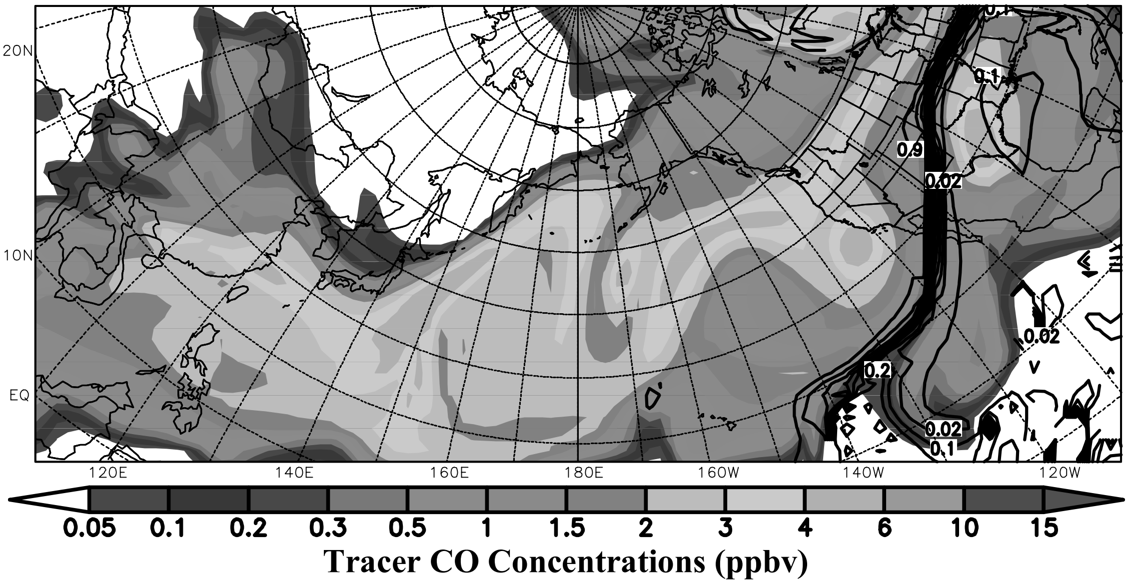

Figure 4. (a–f) Simulated results at 2100 GMT, 25 April 2002. CO Asian ratios are presented with contour lines in Figures 4a and 4b. CO and O_3 budgets are in ppbv/h. See color version of this figure at back of this issue.

observations. Here we show how the various model products can aid in the analysis and how the observations help to evaluate the model performance. These aspects are explored through the analysis of individual flights. The flights discussed above focus on typical flights that involve a mixture of local and Asian influences.

4.1. WP-3 Flight on 25 April

[21] On 25 April the NOAA WP-3 aircraft performed its second flight along the California coast (Figure 4), and encountered aged Asian air masses mixed with American pollutants. In the model's 1-km layer over most of the domain, with the exception of the continental United States, the anthropogenic CO Asian ratio is higher than 0.8 (80%) (Figure 4a). Figure 4b shows that Asian sources have a stronger impact on CO over North America at higher altitudes. Figures 4c and 4d show simulated O_3 over the eastern Pacific and the WP-3 flight path, which was located near a low-pressure system. At low altitudes (Figure 4c), O_3 was formed over the western United States and transported out over the ocean, as shown by the band with $O_3 > 55$ ppbv that extends southwestward from northern California. The oceanic area with $O_3 > 45$ ppbv west of Mexico is associated with an aged polluted air mass composed of a mixture of Asian and North American air (as shown by the Asian ratio <0.6 as shown in Figure 4a). In the higher altitudes, ozone

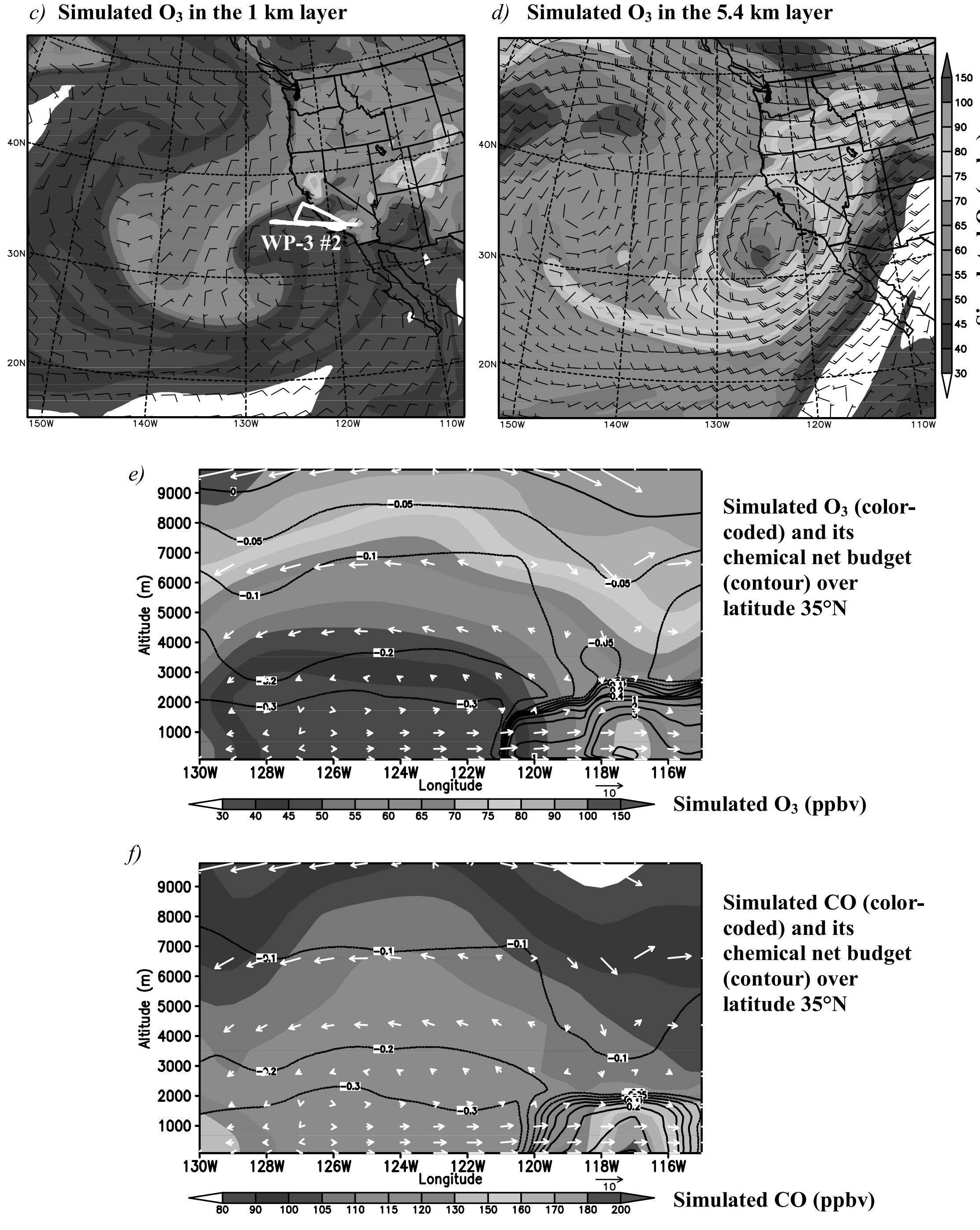
c) **Simulated O_3 in the 1 km layer**

d) **Simulated O_3 in the 5.4 km layer**

e) **Simulated O_3 (color-coded) and its chemical net budget (contour) over latitude 35°N**

Simulated O_3 (ppbv)

f) **Simulated CO (color-coded) and its chemical net budget (contour) over latitude 35°N**

Simulated CO (ppbv)

Figure 4. (continued)

concentrations were mainly maintained by downward transport of stratospheric ozone (Figures 4d and 4e).

[22] Figure 4e shows the cross section of O_3 concentration and chemical net budget along latitude 35°N, a section that approximates the path of WP-3 flight 2. Simulated O_3 showed a net loss over the ocean areas and above 3-km over land, and a net production below ~3 km over the polluted regions near Los Angles. In the low altitudes over the ocean, O_3 had the highest loss rates and lowest concentrations because the high-water-vapor conditions within the marine boundary layer (MBL) benefited the $O^1D + H_2O \rightarrow 2OH$ reaction, which reduced the chance of O^1D converting back to O_3 via $O^1D + Air \rightarrow O^3P$ and $O^3P + O2 \rightarrow O_3$. Because of the high OH production in the MBL the CO net chemical budget was approximately -0.3 ppbv/h (Figure 4f). The CO chemical budget became positive only over the polluted regions where hydrocarbon oxidization was important.

[23] Figure 5 compares measurements of WP-3 flight 2 with simulated values extracted along the flight path. The tracer-CO results are plotted in Figure 5a. The CO Asian ratios varied by height, with values >65% and <40% for the flight altitudes higher than 3 km and lower than 2 km, respectively. Asian air masses are usually transported across the Pacific in the middle to upper troposphere, and brought

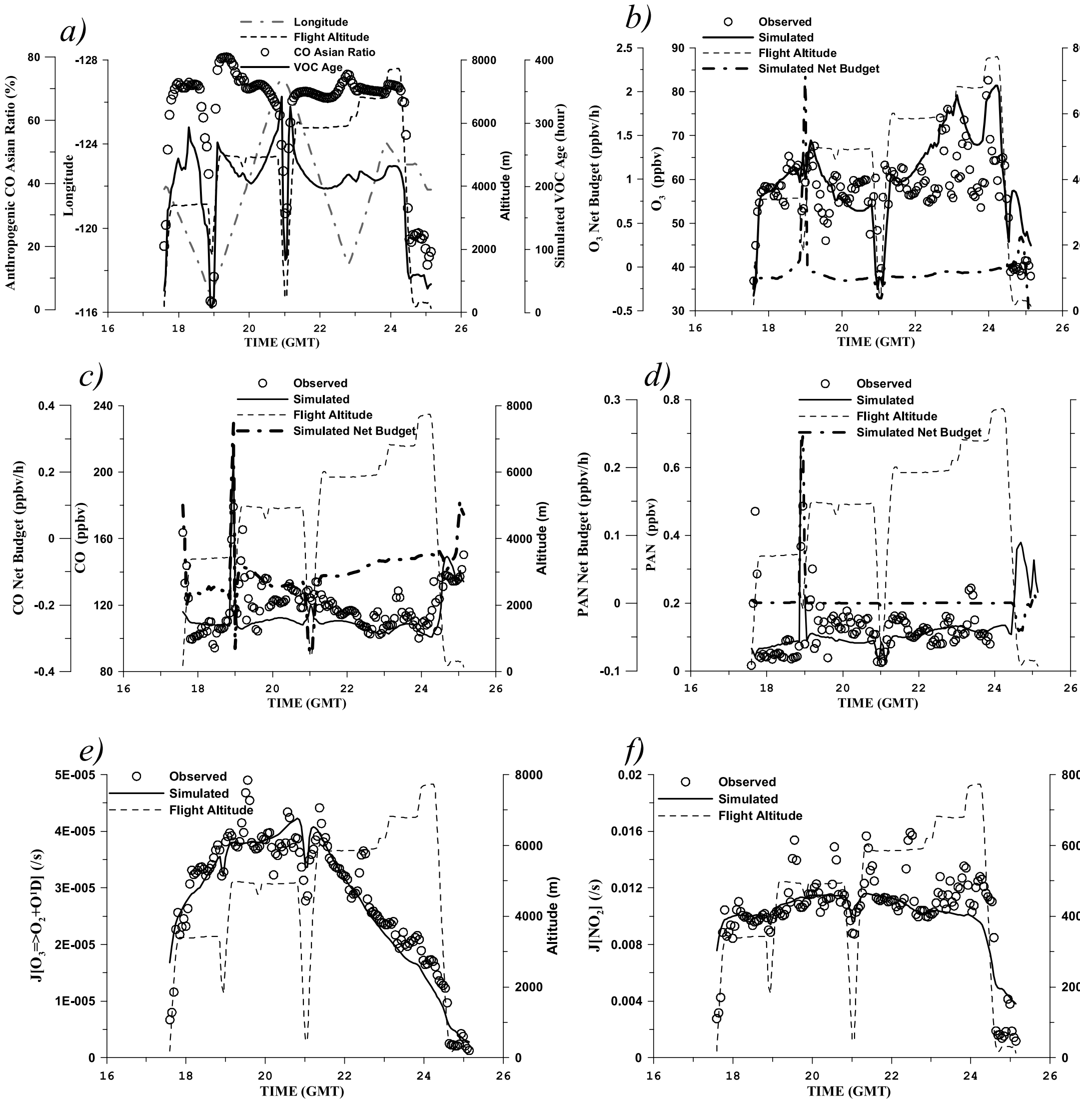

Figure 5. (a–f) STEM simulations compared to measurements for the WP-3 flight on 25 April.

to lower altitudes through convective exchange and subsidence. At low altitudes over inland locations, such as the flight path around 1855 GMT, the CO Asian ratio fell below 10%. For short-lived species, like NO_x and SO_2, the Asian influence is small because of removal and conversion processes during the long-distance transport. Figure 5b shows that the STEM simulation was able to capture the main observed ozone features. The calculated ozone net photochemical budget is also presented and the net budget reached a maximum positive value around 1855 GMT, when the aircraft flew inland at low altitudes. At other flight locations the O_3 chemical budget was negative.

[24] Figure 5c shows that modeled CO exhibits much less variability than that observed, and underestimated the observed CO by more than 10 ppb during 1900–2100 GMT. The calculated CO chemical budget was positive when the pollutant loading was high, reflecting CO produced from nonmethane hydrocarbon (NMHC) oxidation. For other locations the CO budget was always negative and CO consumption via reaction with OH dominated. The chemical net budget for PAN is similar to that of CO. PAN was chemical formed over polluted areas, while photolytic loss was the main reason for the negative budgets at clean locations. Figure 5 also shows that the STEM model accurately predicted J values (photolysis rates) for $J[O_3 \rightarrow O_2 + O^1D]$ and $J[NO_2 \rightarrow NO + O^3P]$ using the online TUV. The agreement between the simulation and measurement for $J[O^1D]$ is better than that for $J[NO_2]$, since $J[NO_2]$ is sensitive to long-wavelength radiation, which can be affected by fractional clouds (a quantity that is difficult to model). This flight encountered some fractional clouds. Figure 5f shows that several of the peak values for $J[NO_2]$ above 4 km were not predicted by the model and these could be associated with fractional clouds. Similar results were found for J values over western Pacific during TRACE-P as discussed by *Tang et al.* [2003a].

[25] To explore the photochemical system during this flight, three points along the flight path were further analyzed. The WP-3 aircraft observations at 1900, 1903, and 2100 GMT were selected. The points at 1900 and 1903 GMT were when the aircraft made a vertical ascent downwind of Los Angles. The model simulation shows disparate

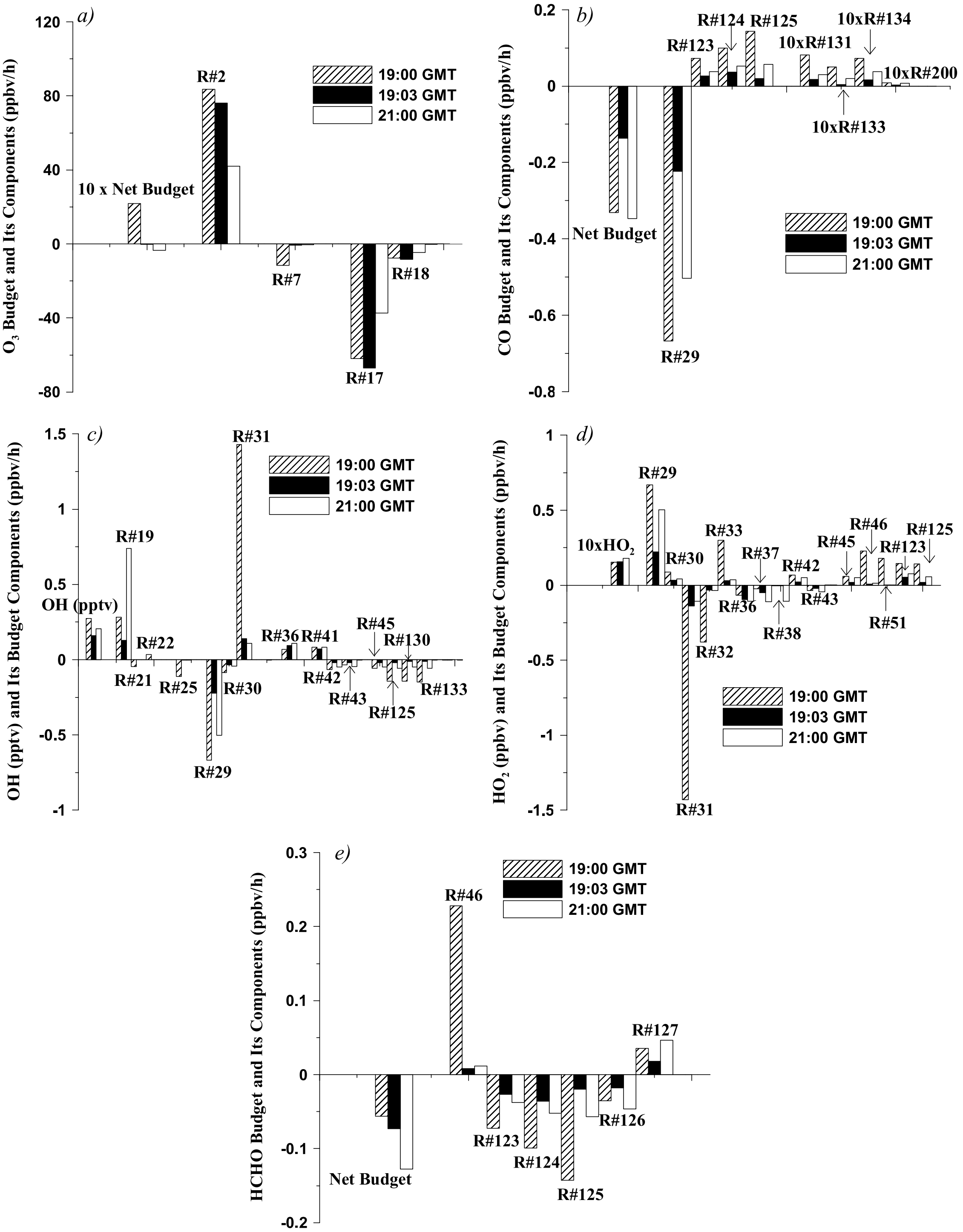

Figure 6. Simulated species budgets and their components for (a) O_3, (b) CO, (c) OH, (d) HO_2, and (e) HCHO at 1900 GMT (altitude 2837 m), 1903 GMT (altitude 3630 m), and 2100 GMT (altitude 470 m) along the WP-3 flight path on 25 April. Some net budgets, concentrations, and rate terms are multiplied a factor of 10 for display purposes. Negative values represent loss terms. For each term, the bar sequence from left to right is 1900 GMT, 1903 GMT, and 2100 GMT. The reactions are listed in Table 2.

air masses at the beginning and end of this profile, with the predicted CO Asian ratio of 10% at 1900 GMT and 64% at 1903 GMT. When air masses from the Pacific Ocean moved onshore during the daytime, an internal boundary layer (IBL) formed [*Garratt*, 1990], which in the model extended to ~2 km. Within the boundary layer the air was mixed with local pollutants transported from Los Angeles and surrounding area. Above this boundary layer, the air preserved its aged Asian features. The point at 2100 GMT was at the west end of this flight at low altitude over the eastern Pacific.

[26] Figure 6 shows the simulated chemical production and loss terms for O_3, CO, OH, HO_2, and HCHO at these

Table 2. Reaction Index as Mentioned in Figure 6

Reaction No.	Reaction[a]
(R2)	$O^3P + O_2 \rightarrow O_3$
(R7)	$O_3 + NO \rightarrow NO_2 + O_2$
(R17)	$O_3 + h\nu \rightarrow O_2 + O^3P$
(R18)	$O_3 + h\nu \rightarrow O_2 + O^1D$
(R19)	$O^1D + H_2O \rightarrow 2OH$
(R21)	$OH + NO \rightarrow HONO$
(R22)	$HONO + h\nu \rightarrow OH + NO$
(R25)	$OH + NO_2 \rightarrow HNO_3$
(R29)	$OH + CO + O_2 \rightarrow HO_2 + CO_2$
(R30)	$OH + O_3 \rightarrow HO_2 + O_2$
(R31)	$HO_2 + NO \rightarrow NO_2 + OH$
(R32)	$HO_2 + NO_2 \rightarrow HNO_4$
(R33)	$HNO_4 + h\nu \rightarrow 0.61HO_2 + 0.61NO_2 + 0.39OH + 0.39NO_3$
(R36)	$HO_2 + O_3 \rightarrow OH + 2O_2$
(R37)	$HO_2 + HO_2 \rightarrow H_2O_2 + O_2$
(R38)	$HO_2 + HO_2 + H_2O \rightarrow H_2O_2 + O_2 + H_2O$
(R41)	$H_2O_2 + h\nu \rightarrow 2OH$
(R42)	$H_2O_2 + OH \rightarrow HO_2 + H_2O$
(R43)	$HO_2 + OH \rightarrow O_2 + H_2O$
(R44)	$OH + SO_2 + H_2O + O_2 \rightarrow H_2SO_4 + HO_2$
(R45)	$H_2 + OH \rightarrow HO_2$
(R46)	$CH_3O_2 + NO + O_2 \rightarrow NO_2 + HCHO + HO_2$
(R51)	$RO_2\_R + NO \rightarrow NO_2 + HO_2$
(R123)	$HCHO + h\nu + 2O_2 \rightarrow 2HO_2 + CO$
(R124)	$HCHO + h\nu \rightarrow CO + H_2$
(R125)	$OH + HCHO \rightarrow HO_2 + CO$
(R126)	$HCHO + HO_2 \rightarrow HOCOO$
(R127)	$HOCOO \rightarrow HCHO + HO_2$
(R130)	$CH_3CHO + OH \rightarrow CCO\_O_2$
(R131)	$CH_3CHO + h\nu \rightarrow CO + HO_2 + CH_3O_2$
(R133)	$RCHO + OH \rightarrow 0.034CO + 0.034CH_3CHO + Other$
(R134)	$RCHO + h\nu \rightarrow CH_3CHO + CO + HO_2 + RO_2\_R$
(R200)	$C_2H_2 + OH \rightarrow 0.603OH + 0.297HO_2 + 0.393CO + 0.1RO_2\_R + 0.096HCHO$

[a] RCHO represents lumped aldehydes with three and more carbons, RO_2_R is the peroxy radical operator representing the NO to NO_2 conversion with HO_2 formation, and CCO_O_2 represents acetyl peroxy radicals [*Carter*, 2000].

three points. The O_3 budget components (Figure 6a) show that O_3 had a positive budget and the highest photochemical generation through $O^3P + O_2 \rightarrow O_3$ (reaction (R2) in Table 2) at 1900 GMT in the polluted air mass. O_3 also had a lower photolysis rate (reactions (R17) and (R18) in Table 2) at 1900 GMT than at 1903 GMT because of the altitude dependency of the actinic flux. At 1903 GMT the O_3 net budget was near zero. When the WP-3 aircraft flew at low altitude over the clean oceanic area at 2100 GMT the O_3 budget was negative because of the rapid consumption of O^1D in the water-rich MBL via $O^1D + H_2O \rightarrow 2OH$ (reaction (R19) in Table 2), as was also discussed for Figure 4e.

[27] Under these conditions there is higher OH production (Figure 6c) and CO net loss (Figure 6b) at 2100 GMT. Figure 4b shows that the polluted air mass encountered at 1900 GMT had the highest CO consumption through reaction (R29), CO + HO + $O_2 \rightarrow HO_2 + CO_2$, because of its high OH and CO concentrations. However, this polluted point also had the highest CO production among these three points because of oxidation and photolysis of aldehydes. The simulation indicates that most of the aldehydes were intermediate products of hydrocarbon oxidization at 1900 GMT, and that the hydrocarbon oxidation offset part of CO loss, resulting in a net positive CO budget in the polluted area (Figure 4f). The two clean locations at 1903 GMT and 2100 GMT had similar low concentrations for most hydrocarbons and aldehydes, but the OH production in the MBL at 2100 GMT was high, resulting in the highest CO net loss among these three points.

[28] Figure 6c shows that the polluted point of 1900 GMT had the highest OH concentration, mainly because of the additional OH production through reaction (R31), NO + $HO_2 \rightarrow OH + NO_2$. In polluted areas the following reactions are important:

$$CO + OH + O_2 \rightarrow HO_2 + CO_2, \tag{R29}$$

$$HO_2 + NO \rightarrow NO_2 + OH, \tag{R31}$$

$$NO_2 + h\nu \rightarrow NO + O^3P, \tag{R1}$$

$$O^3P + O_2 \rightarrow O_3, \tag{R2}$$

$$O_3 + h\nu \rightarrow O_2 + O^1D, \tag{R18}$$

$$O^1D + H_2O \rightarrow 2OH. \tag{R19}$$

This series of reactions is constrained by NO_x and NMHC concentrations. Under optimal NO_x and NMHC conditions these reactions effectively produce OH. The point at 1900 GMT reflects this situation, and high OH concentrations were observed downwind of Los Angeles, which will be discussed later. Under low-NO_x conditions these reactions cannot be performed completely, and Figure 6c shows that the reaction rates of reaction (R31) at 1903 GMT and 2100 GMT were much lower than that at 1900 GMT. The reaction rate of reaction (R19) was highest at 2100 GMT because of its rich water vapor, which resulted in elevated OH concentrations, though still lower than that at the polluted point. At the polluted point OH increased by converting HO_2 to OH. Here HO_2 concentrations were maintained (Figure 6d) by HO_2 production via reactions (R46), (R51), (R123), and (R125) that converted RO_2 and HCHO to HO_2. RO_2 and HCHO were produced as intermediate products of hydrocarbon oxidization. Figure 6d shows that the MBL site had the highest HO_2 concentration, due to high OH (for reaction (R29)) and low NO_x (for reaction (R31)) concentrations. Figures 6c and 6d illustrate the impact of fast conversion between OH and HO_2, and their connection to external sources. Reaction (R19) was the main external source for HO_x at the MBL, and RO_2 and aldehydes were the main precursors of HO_x at the polluted site.

[29] Figure 6e shows that HCHO had negative budgets at all these sites, and the MBL site had the highest HCHO net loss because of its high OH. The polluted point at 1900 GMT had the highest HCHO consumption, but it also had the highest HCHO production from hydrocarbon oxidization. At the clean points HCHO mainly came from methane oxidization $CH_4 + OH + O_2 \rightarrow CH_3O_2 + H_2O$ and $CH_3O_2 + NO + O_2 \rightarrow NO_2 + HCHO + HO_2$ (reaction (R46) in Table 2), which was constrained by NO_x availability. Other production pathways, such as $CH_3O_2 + CH_3O_2 \rightarrow CH_3OH + HCHO + O_2$, were usually small. The production of HCHO was not sufficient to offset HCHO consumption except in heavy polluted areas. At the 1900 GMT point the

pollutants were already diluted, and the HCHO net chemical budget was negative.

4.2. WP-3 Flight on 15 May

[30] The eleventh NOAA WP-3 flight flew west to 129°W over the eastern Pacific on 15 May (Figure 7). This flight encountered aged Asian and American air masses. Figure 7a shows that CO Asian ratio was high over most of the eastern Pacific in the model's 1-km layer. Some fresh air masses with Asian CO > 15 ppbv approached this region, but did not arrive at the WP-3 flight path. Along the North American coastline, CO Asian ratios showed a strong gradient. At 5.4 km (Figure 7b) the CO Asian ratio was higher than 0.9 throughout the domain north of 30°N, which reflects the high transport efficiency in midlatitudes to high latitudes and high altitudes. The influence of American sources was concentrated to inland areas at low altitudes. The WP-3 flight region was ahead of a cold front, and north winds dominated (Figures 7c, 7d, and 7e). The prefrontal ascending winds transported low O_3 concentrations from the MBL to higher altitudes, and the postfrontal descending air caused a high-O_3 zone around 155°W, 44°N, which was shown in all the layers (Figures 7c, 7d, and 7e). It should be noted that the relatively fresh Asian air masses (northwest corner of this domain) were also transported mainly from the high altitudes because of the high transport efficiency.

[31] Figures 7f, 7g, and 7h show the O_3 chemical net budget in the 1-km, 2.8-km, and 5.4-km layers. In the l-km layer O_3 net production was high over polluted inland areas and in the fresh Asian air masses (Figure 7f). The distribution of O_3 concentrations (Figure 7c) shows high concentrations in regions with positive net budgets, indicating that the O_3 chemical budget was the dominant factor affecting O_3 concentrations in the low altitudes. In the 2.8-km layer, transport effects were important as shown by the fact that the O_3 chemical net budget was negative (less than -0.1 ppbv/h) over most of California, but O_3 concentrations were still higher than background (>65 ppbv) over most Southern California. In the 5.4-km layer, transport effects dominated. Figure 7h shows that the O_3 net budget was negative over most of this domain, but very high O_3 concentrations (>100 ppbv) existed in some areas because of the stratospheric influence. Under these conditions, elevated O_3 levels can correspond to areas with strong O_3 loss caused by photolysis, such as the high-O_3 zone around 112°W, 48°N.

[32] The CO net budget distribution is similar to O_3 in the 5.4-km layer, as O_3 loss is mainly through its photolysis process, and the O^1D produced forms OH (via reaction (R19) in Table 2), which consumes CO. Under these conditions O_3 loss is usually correlated with CO loss. Figures 7i, 7j, and 7k show that the CO net budget is positive only over heavily polluted areas and their downwind sites rich in hydrocarbons. At high altitudes the CO budget was always negative.

[33] WP-3 flight 11 flew a triangle flight path over the eastern Pacific (Figure 7f), with its west end longitude reaching about 129°W. In contrast to WP-3 flight 2, this flight had some low-altitude points with possible strong Asian signals (compare 2050 GMT, Figure 8a). At higher altitudes (>3 km) the CO Asian ratio was greater than 0.8. Figure 8a shows that the CO Asian ratio was lower than 30% only in the low-altitude near-coast flight segments. The STEM simulated CO agrees well with the observations (Figure 8b), and the simulated CO budget shows that net CO production occurred only in the departing and arriving segments, near the polluted San Francisco bay area.

[34] Figure 8c shows the O_3 concentration comparison and simulated O_3 net chemical budget. The calculated ozone captured many of the large-scale features (including the altitude dependency), but was not able to resolve the finer-scale features observed. The simulated O_3 net chemical budget for this flight is similar to that of flight 2. The model accurately captured ethyne values as shown in Figure 8d. Since ethyne has no photochemical sources its net chemical budget is always negative, and mainly determined by local OH concentrations, even over polluted area. The variation of ethyne chemical budget is very similar to that of CO over ocean since both are determined by the OH concentration. The OH concentration was very sensitive to photolysis rate, and the model reasonably simulated the observed J value behavior (Figures 8e and 8f). Most of the areas that WP-3 flight 11 flew over were under clear-sky conditions, and the photolysis rates were mainly affected by altitude and sunlight zenith angle. Figure 8g shows the comparison for PAN concentrations and the simulated PAN chemical budget, which are similar to those for O_3 (Figure 8c). The PAN formation is mainly through photochemical reaction between NO_x and NMHCs, and its loss is mainly caused by its photolytic destruction.

[35] WP-3 flights 2 and 11 represent the situation typically encountered by most flights over the eastern Pacific and the near-coast regions. In these flights Asian air masses impacted by Asian sources dominated at altitudes above 4 km, but had little effect over the inland low-altitude areas. Since aged air masses usually were low in NO_x, the O_3 photochemical production was low, and the net chemical budgets were negative in the Asian air masses arriving over North America.

5. Nitrate Partition

[36] *Tang et al.* [2004] discussed nitrate partitioning between the gas and aerosol phases for the ACE-Asia and TRACE-P experiments, and found that the regional model without aerosol considerations tended to overestimate nitrate acid (HNO_3). Similar results [*Neuman et al.*, 2003] were found for the ITCT 2K2 flights along the coast where regional pollutants interacted with sea salt, resulting in some of the nitric acid partitioning into the sea-salt particles. Figure 9 shows the simulated HNO_3 mixing ratios with and without aerosol uptake compared to the measurements for WP-3 flights 4, 5, 8, and 9. The simulation with aerosol uptake had lower HNO_3 concentrations than the simulation without aerosol for most segments of these flights. Because of the relatively coarse horizontal resolution, the simulation with aerosol underestimated most of the HNO_3 peak values. The most significant differences between these two simulations appear for the predictions for background HNO_3 levels. The simulation without aerosol uptake systematically overestimated the low background concentrations, especially for WP-3 flight 5, and it overestimated the HNO_3 peak value for WP-3 flight 4. Under cation-limited conditions, the simulation with aerosol uptake can yield higher HNO_3 values (Figure 9b) because of competition effects involving sulfates.

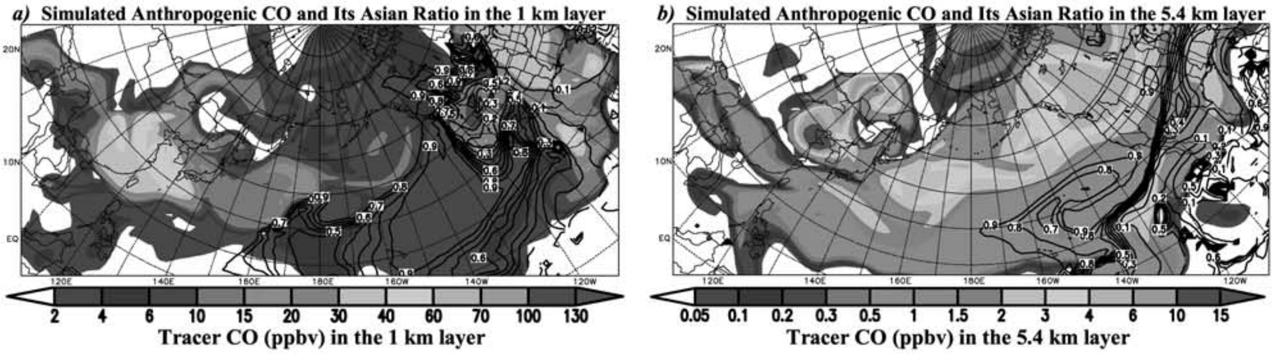
a) **Simulated Anthropogenic CO and Its Asian Ratio in the 1 km layer**

b) **Simulated Anthropogenic CO and Its Asian Ratio in the 5.4 km layer**

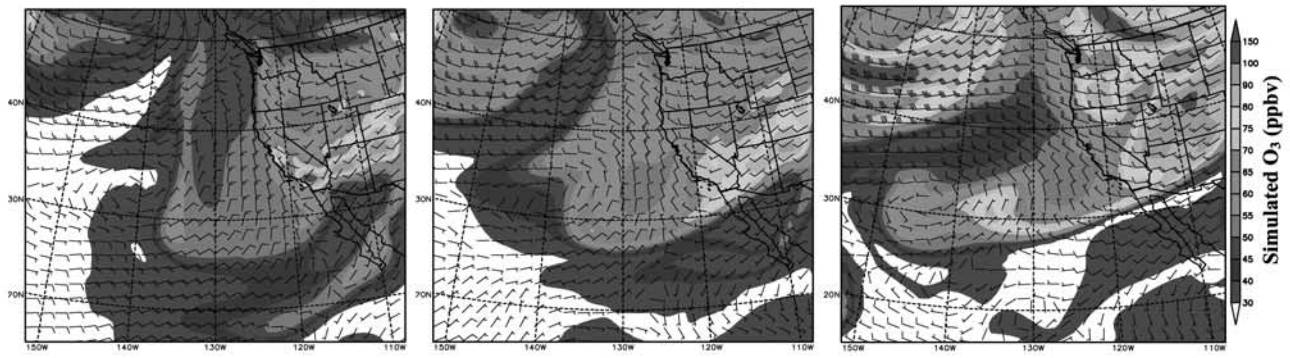
c) **Simulated O_3 in the 1 km layer**

d) **Simulated O_3 in the 2.8 km layer**

e) **Simulated O_3 in the 5.4 km layer**

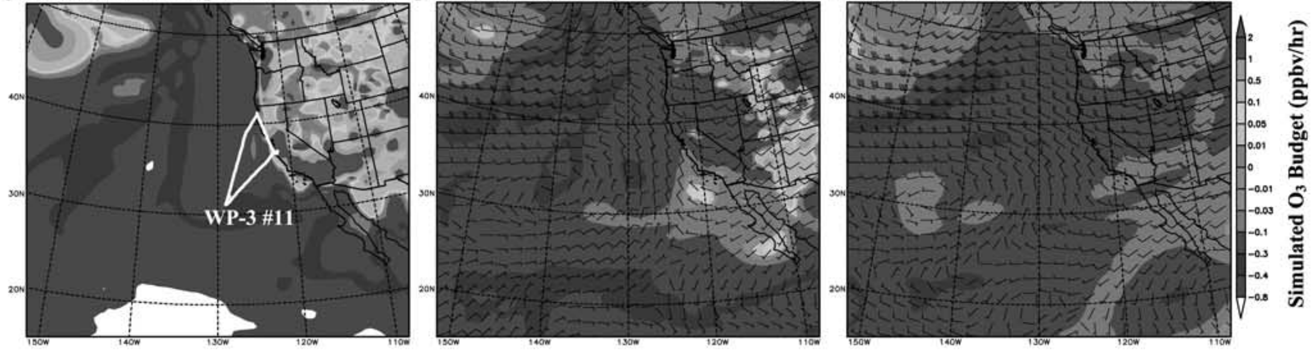
f) **Simulated O_3 Budget in the 1 km layer**

g) **Simulated O_3 Budget in the 2.8 km layer**

h) **Simulated O_3 Budget in the 5.4 km layer**

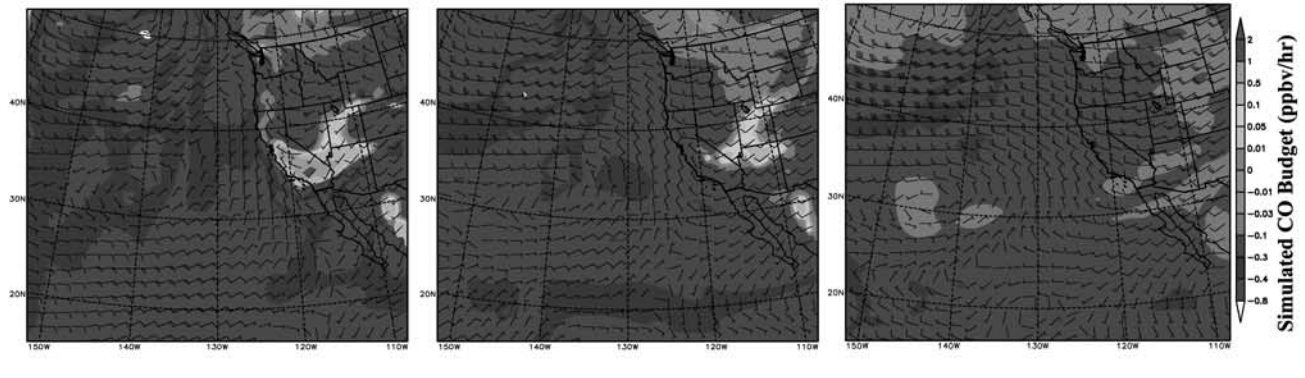
i) **Simulated CO Budget in the 1 km layer**

j) **Simulated CO Budget in the 2.8 km layer**

k) **Simulated CO Budget in the 5.4 km layer**

Figure 7. (a–k) Simulated results at 2100 GMT, 15 May 2002. CO Asian ratios are presented with contour lines in Figures 7a and 7b. See color version of this figure at back of this issue.

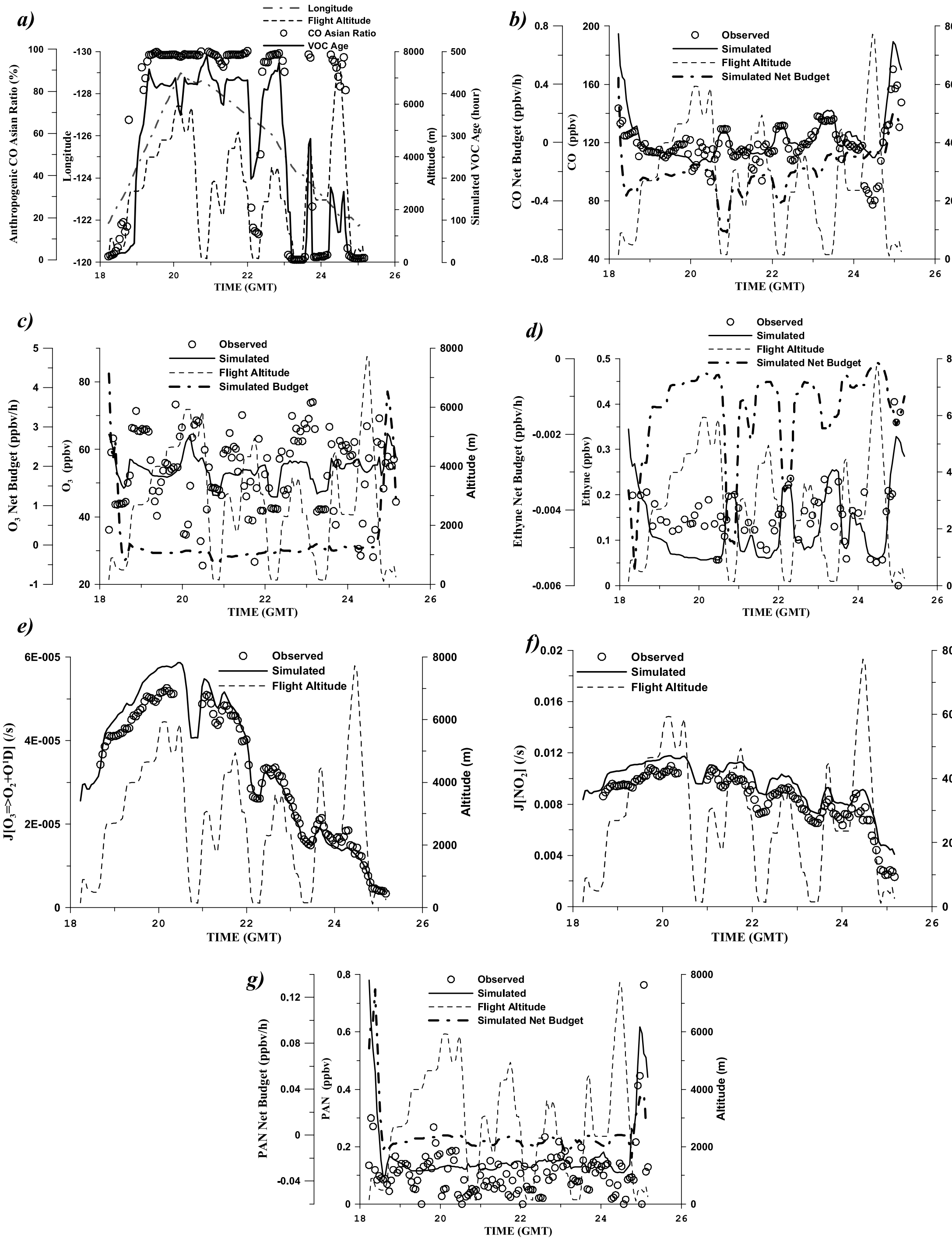

Figure 8. (a–g) STEM simulations compared to measurements for the WP-3 flight on 15 May.

However, over most clear oceanic sites, aerosol uptake tended to reduce gas-phase HNO_3. This partitioning is an important factor causing the very low NO_y ratio in the long-distance-transported Asian air masses (Figures 2a and 2b).

6. Nested Simulation for the Los Angeles Plume

[37] WP-3 flight 10 performed an urban plume study over Los Angeles (LA) and surrounding areas. For this flight the contribution of Asian sources were small. The primary domain over the eastern Pacific (Figure 1) with its 60-km horizontal resolution was not able to capture the fine structures caused by local emissions. *Tang* [2002] tested the multiscale simulation using nested domains in Nashville, Tennessee, and found that nesting predictions could better reflect power plant and urban plume structures. When the tenth WP-3 flight flew over LA and its downwind areas it encountered strong local plumes with steep concentration gradients, implying that local emissions played the dominant role on species concentrations. To simulate this sce-

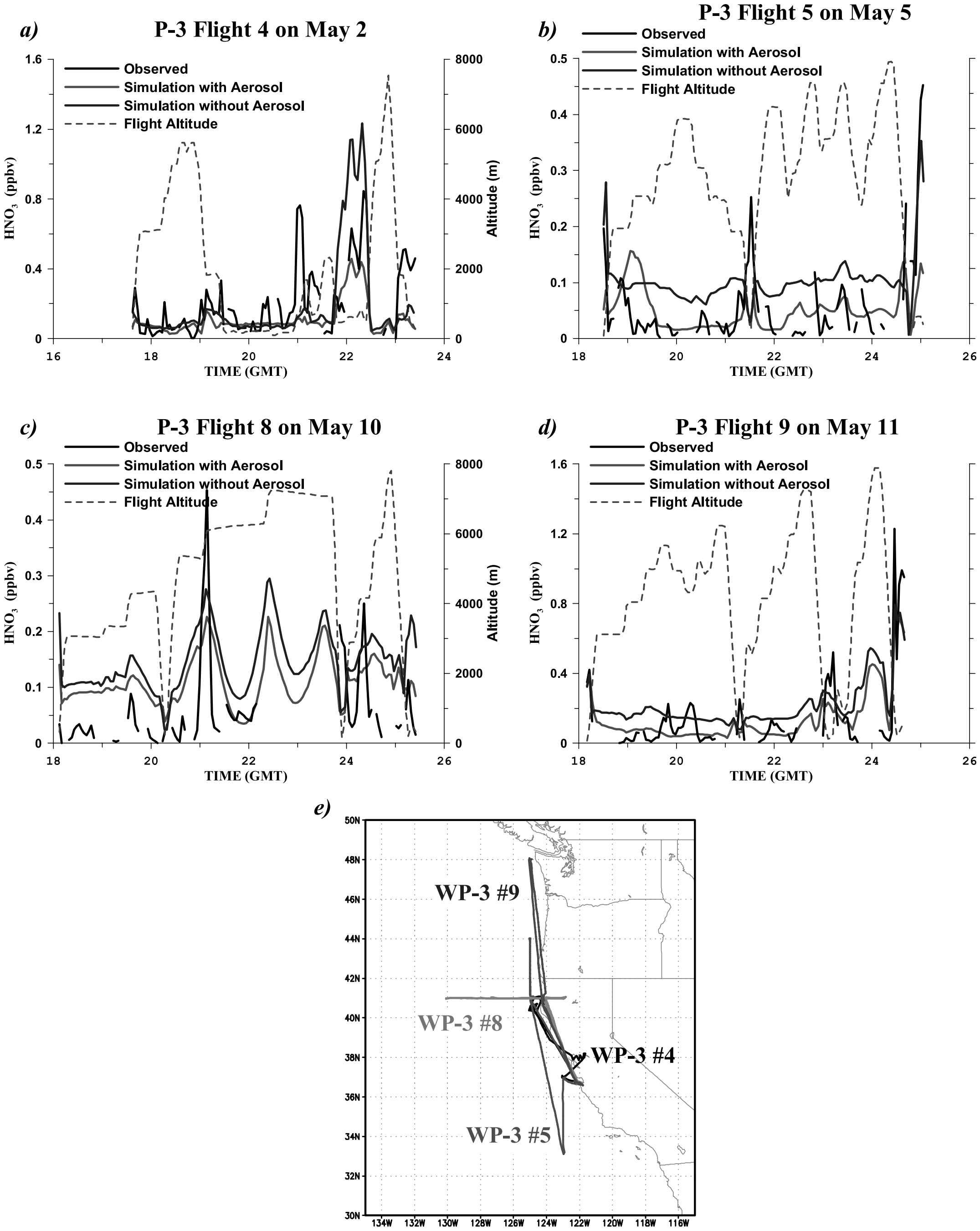

Figure 9. (a–e) STEM simulations with and without the aerosol consideration compared to observations of four WP-3 flights, whose paths are shown in Figure 9e. See color version of this figure at back of this issue.

nario, a domain with a 12-km horizontal nested grid within the primary eastern Pacific domain (Figure 1) was used. Simulated CO and O_3 concentrations in the coarse and fine domains are shown in Figure 10. The coarse and fine simulations produced qualitatively similar CO and O_3 distributions, but the higher resolution highlights the fine-scale structures. During this flight a front passed over LA region. Figure 10a shows that the low-altitude winds came from the northwest and turned southwesterly after passing over LA. In the upwind areas, west of longitude 119°W, the coarse and nesting simulations did not show significant differences for O_3 and CO. Over and downwind of LA the nesting simulated CO showed two high zones (Figure 10a), while the coarse simulation had only one broad high-CO region (Figure 10b). The CO distributions mainly reflect the local emissions and transport effects. The elevated O_3 regions in the nested-grid simulated did not overlap with the peak values of CO (as was the case for the coarse simulation), but instead were shifted downwind. The region of high ozone (>120 ppbv) was significantly smaller on the fine grid, indicating the effect of model resolution on photochemical processes.

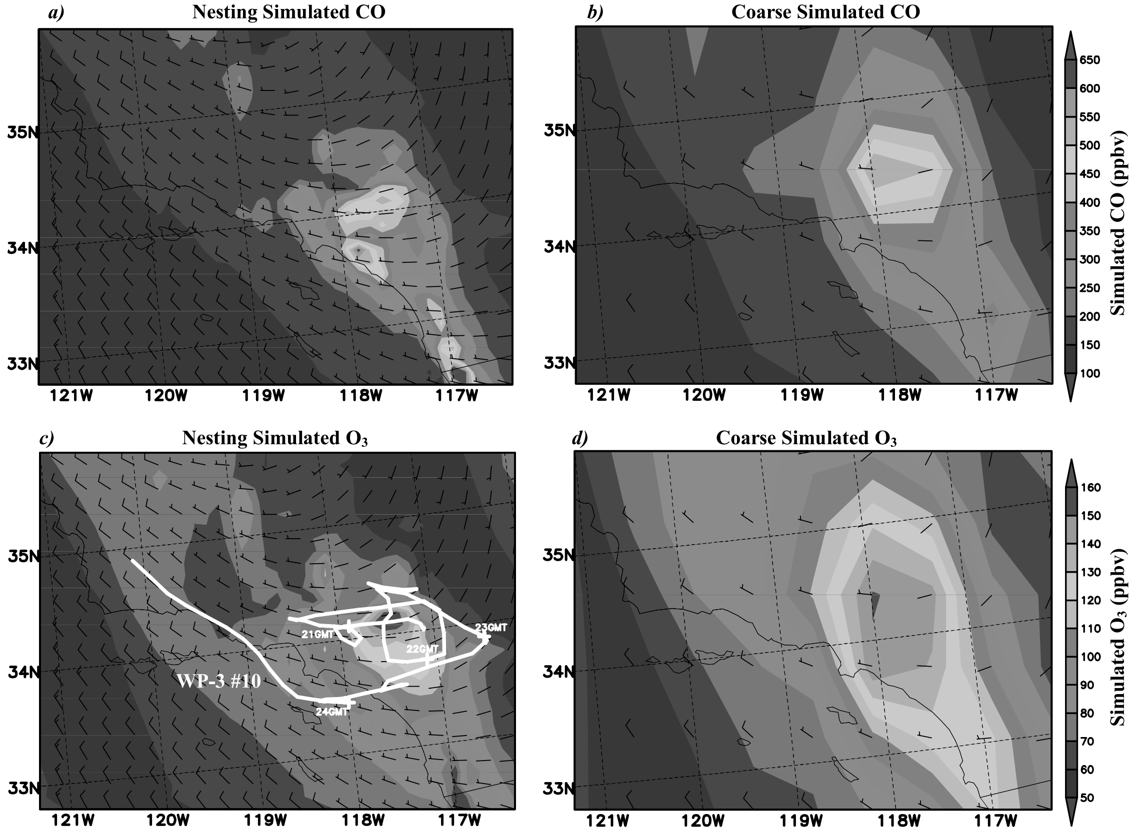

Figure 10. (a–d) Nested (12-km resolution) and coarse (60-km resolution) simulated CO and O_3 at 400 m at 2100 GMT, 13 May, for WP-3 flight 10 over Los Angeles and the surrounding area. See color version of this figure at back of this issue.

[38] To highlight the differences between these two simulations, the flight segment shown in Figure 10c, where the WP-3 aircraft operated around in and around LA, was analyzed further. Figure 11 shows these two simulations compared to the aircraft measurements. The simulated ethyne and propane concentrations using the nested grid were in much better agreement with the observations (Figures 11a and 11b). This is mainly due to the better resolution of the emissions, which enables a better representation of peak values. The refined high-resolution emissions better resolve the differences among urban, suburban and rural areas.

[39] The lifetime of CO is much longer than ethyne or propane, and it also has a higher background concentrations and stronger emissions. Thus CO concentrations reflect the impacts of both local emissions and transport. Both the coarse and fine grid simulated CO capture the main altitude variations (Figure 11c), but the nested grid better represents the CO fine structures. Figure 11c also shows the simulated CO chemical net budgets, which vary in a manner consistent with that for the CO concentrations. The CO chemical budget is determined by the oxidations of CO and hydrocarbons. In the low-altitude areas around LA, hydrocarbons were elevated and CO had a positive net chemical budget that was positively correlated with the hydrocarbon concentrations. Most primary hydrocarbons tend to be coemitted with CO in this region, and thus high CO concentrations usually correspond to high hydrocarbon concentrations (Figures 11a, 11b, and 11c). This is the reason why the CO net budget was correlated with CO concentration. For this flight the CO positive chemical budget helped to maintain the high CO concentration, but the high CO was mainly caused by strong emissions. The contribution of the CO chemical budget to CO concentrations was relatively weak, less than 2.5 ppbv/h (Figure 11c).

[40] Both the fine and coarse grid simulations tended to overestimate O_3 concentration, but the nested one shows better agreement with the observations (Figure 11d). The net O_3 chemical budget for most of the flight segments was positive, up to 25 ppbv/h. For the flight segment after 2140 GMT the O_3 concentrations followed the variations in the O_3 chemical net budgets, implying that O_3 production was the dominant influencing factor for O_3 concentrations (as expected). The O_3 chemical budgets on the fine grid show larger absolute values and variation than for the coarse grid, consistent with the better ability to resolve plume-like structures using the finer grid. The 12-km simulation improved the O_3 prediction, but even finer grids are needed.

[41] The improvement in ozone prediction with finer grids can be explained by looking at the predicted and observed NO_z (NO_y-NO_x) concentrations (Figure 11e). As the photochemical product of NO_x, NO_z is usually highly correlated with O_3 [*Trainer et al.*, 1993]. The fine grid simulation shows a much better agreement with the observations, and the coarse grid tends to overestimate NO_z. Figure 11e also shows the O_3/NO_z ratios. Both simulations

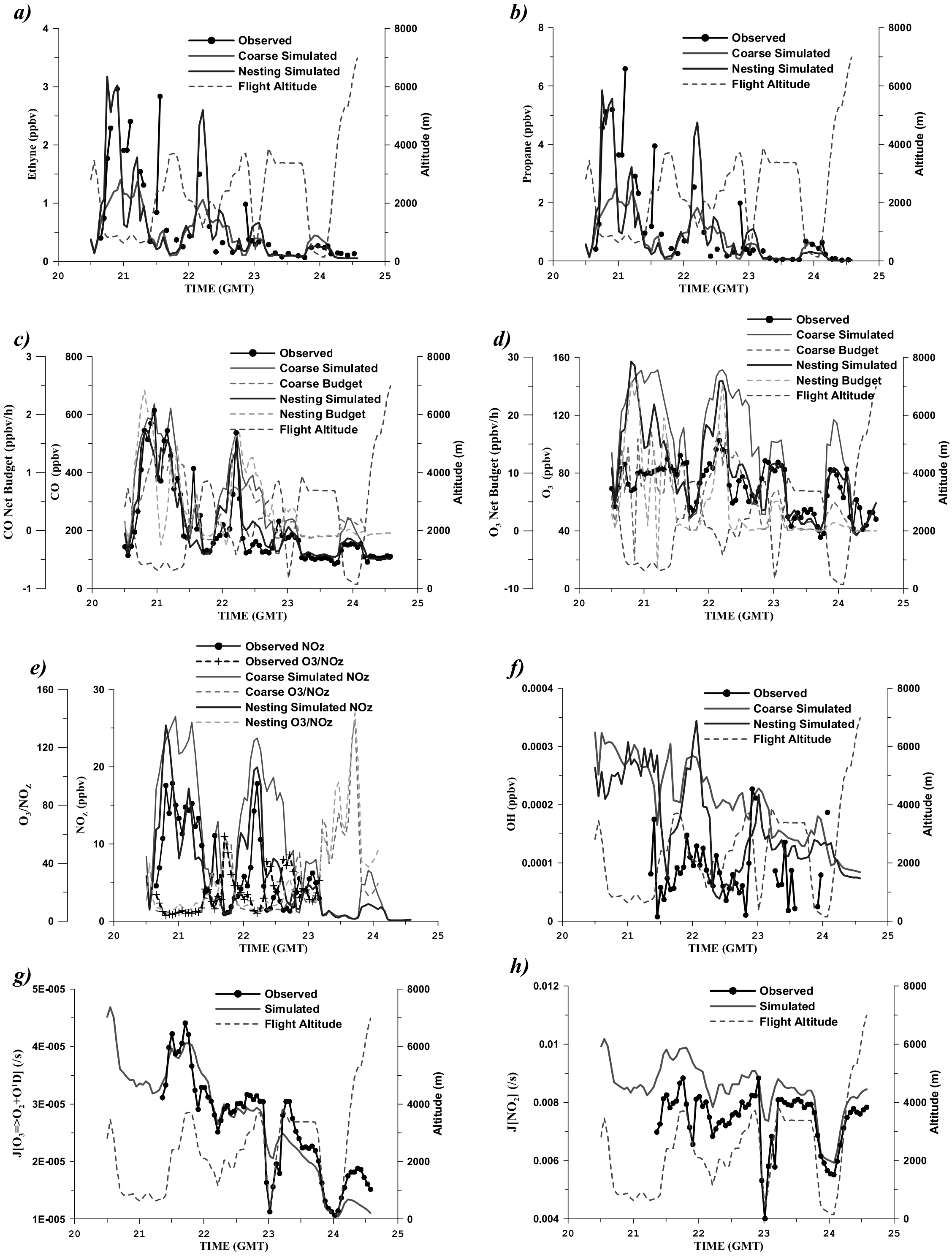

Figure 11. (a–h) Simulations compared to the measurements along the path of WP-3 flight 10 shown in Figure 10c. The nested and coarse simulations have similar *J* value predictions. So Figures 11g and 11h show only one simulation. See color version of this figure at back of this issue.

agree well with the observations for the flight segment before 2200 GMT, but tend to underestimate this ratio (especially for the coarse simulation) by overestimating NO_Z between 2200 GMT and 2300 GMT. The OPE difference between these two simulations and the observations reflect their different photochemical behaviors, which is also highlighted by their OH differences (Figure 11f). Both simulations systematically overestimated OH, but the nested simulation showed improvement for some flight segments (e.g., 2230–2330 GMT). However, the OH overestimation

Table 3. Observed and Simulated (60-km Resolution) Mean Values and Their Correlation Coefficients *R* for ITCT 2K2: All WP-3 Flights

	Below 1 km			1 km to 3 km			Above 3 km		
Species and Variables	Observed	Modeled	*R*	Observed	Modeled	*R*	Observed	Modeled	*R*
Pressure, hPa	971.5	963.1	0.96	801.2	798.5	0.99	554.4	551.7	0.99
Wind speed, m/s	8.2	8.4	0.67	8.0	7.3	0.68	12.7	11.5	0.88
Relative humidity, %	68.8	58.3	0.82	28.8	33.9	0.85	27.5	28.2	0.73
CO, ppbv	154	163	0.92	135	147	0.60	120	113	0.18
O_3, ppbv	47.2	58.1	0.81	57.3	57.8	0.66	59.8	64.0	0.47
Ethane, ppbv	1.62	1.52	0.82	1.31	1.15	0.22	0.98	0.77	0.40
Propane, ppbv	0.60	0.36	0.83	0.32	0.22	0.34	0.13	0.06	0.30
Ethyne, ppbv	0.33	0.34	0.86	0.23	0.23	0.47	0.16	0.11	0.14
SO_2, ppbv	0.76	0.23	0.52	0.44	0.35	0.41	0.30	0.10	0.18
Acetone, ppbv	1.03	0.71	0.89	1.20	0.55	0.64	0.89	0.27	0.28
PAN, ppbv	0.16	0.57	0.68	0.44	0.47	0.06	0.14	0.15	0.26
NO_2, ppbv	1.76	1.04	0.88	0.58	0.49	0.65	0.055	0.018	0.43
NO, ppbv	0.52	0.31	0.83	0.15	0.13	0.69	0.019	0.009	0.43
HNO_3, ppbv	0.80	0.65	0.87	0.81	0.64	0.73	0.13	0.12	0.60
NO_y, ppbv	3.3	3.8	0.92	1.75	2.54	0.66	0.42	0.42	0.51
NO_z, ppbv	1.64	2.46	0.95	1.25	1.92	0.66	0.38	0.40	0.57
Toluene,[a] ppbv	0.113	0.102	0.91	0.0492	0.0604	0.69	0.019	0.017	0.18
Xylene,[a] ppbv	0.150	0.051	0.85	0.0279	0.0195	0.73	0.0047	0.0035	0.20
$J[NO_2]$, 1/s	6.66×10^{-3}	7.62×10^{-3}	0.67	9.1×10^{-3}	8.83×10^{-3}	0.58	0.010	0.0092	0.56
$J[O_3 \rightarrow O_2 + O^1D]$, 1/s	2.00×10^{-5}	2.30×10^{-5}	0.86	2.92×10^{-5}	2.77×10^{-5}	0.84	2.95×10^{-5}	2.77×10^{-5}	0.83
$J[H_2O_2]$, 1/s	4.31×10^{-6}	5.75×10^{-6}	0.79	6.21×10^{-6}	6.88×10^{-6}	0.74	6.72×10^{-6}	7.10×10^{-6}	0.77
$J[HNO_3]$, 1/s	3.67×10^{-7}	4.94×10^{-7}	0.84	5.34×10^{-7}	5.93×10^{-7}	0.81	5.47×10^{-7}	5.90×10^{-7}	0.83
$J[HNO_2 \rightarrow OH + NO]$, 1/s	1.46×10^{-3}	1.49×10^{-3}	0.68	2.02×10^{-3}	1.73×10^{-3}	0.60	2.26×10^{-3}	1.81×10^{-3}	0.59
$J[HCHO \rightarrow H + HCO]$, 1/s	1.87×10^{-5}	2.49×10^{-5}	0.81	2.75×10^{-5}	3.05×10^{-5}	0.77	3.20×10^{-5}	3.37×10^{-5}	0.79
$J[HCHO \rightarrow H_2 + CO]$, 1/s	3.13×10^{-5}	3.58×10^{-5}	0.74	4.65×10^{-5}	4.33×10^{-5}	0.69	5.58×10^{-5}	4.70×10^{-5}	0.69

[a] Measured with proton-transfer-reaction mass spectrometry (PTR-MS).

is not caused by overprediction of the *J* values. Figures 11g and 11h show $J[O_3 \rightarrow O_2 + O^1D]$ and $J[NO_2]$ simulations compared to the observations. $J[O_3 \rightarrow O_2 + O^1D]$ is a key factor for clear-background OH, since $O^1D + H_2O \rightarrow 2OH$ (reaction (R19) in Table 2) is the primary natural source of OH. The simulation agrees well with the observations for $J[O_3 \rightarrow O_2 + O^1D]$, but overestimates $J[NO_2]$. However, the $J[NO_2]$ overestimation is much smaller than the OH or O_3 overestimations for the flight segments before 2300 GMT, indicating that OH overestimation may be associated with other process. The observed peak of OH appeared downwind of LA at low altitude (2300 GMT in Figure 11f) where the observed *J* values were very low (Figures 11g and 11h). This implies that other photochemical processes had stronger influence on OH than the reaction (R19) only in the polluted area, which was also discussed before (Figure 6). *Tang* [2002] showed that nested simulation could have different photochemical relationship from the corresponding coarse simulation. In this WP-3 flight segment, these two simulations showed different responses to the same *J* values, because of their different pollutant loadings. Figure 11 shows that the nested simulation yielded better agreement with the observation than the coarse one for most flight segments, implying the impacts of changing resolution on emitted species, secondary generated species, and the photochemical system.

7. Mission-Wide Summary

[42] The aircraft observations provide a valuable data set upon which to evaluate the models capabilities to simulate trace species distributions in the eastern Pacific. A mission-wide summary of the model predicted and observed values are shown in Table 3. Presented are mean values for all 3-min-averaged observations and simulated values for the 13 WP-3 flights parsed into and averaged over three altitude layers. Also shown are the correlation coefficients *R*. The RAMS model driven by NCEP reanalysis data accurately represented the meteorological variables as shown for pressure, wind speed and relative humidity. In terms of trace gas species the highest mean concentrations are generally found below 1 km, indicative of the fact that low-altitude flights tended to sample air dominated by emissions from North America. PAN, HNO_3, and acetone showed highest concentrations in the 1–3-km layer, and O_3 (peak value >3 km) are the exceptions. The model performed best in the lower altitudes, and for primary emitted species such as CO, ethane, propane, NO_2, NO, and toluene. All species with the exception of SO_2 and xylene are predicted within a factor of 2, and many within a factor of 1.2. The correlation coefficients for all the listed species are greater than 0.67. The predictions for the 1–3-km region for SO_2, O_3, NO_z are usually better than the <1-km layer values in terms of mean values reflecting the fact that this layer is not so heavily impacted by the very local sources. However, *R* values are lower. The predictions >3 km are markedly poorer, with *R* values typically lower than 0.5. *J* values are a notable exception, and are predicted with appreciable skill at all altitudes. *J* value predictions mainly reflected the simulations for aerosol optical properties and clouds. $J[NO_2]$ is very sensitive to fractional cloud, and the correlation coefficients for it are relatively low compared to predictions for other *J* values.

[43] The values presented in Table 3 are a mixture of North-American- and Asian-emission-influenced air masses. To further evaluate the model performance, the data were stratified using model-calculated Asian ratios. The statistics for data points with Asian ratios <20% and

Table 4. Observed and Simulated (60-km Resolution) Mean Values and Their Correlation Coefficients *R* for ITCT 2K2: WP-3 Flights With CO Asian Ratio <20%

	Below 1 km			1 km to 3 km			Above 3 km		
Species and Variables	Observed	Modeled	*R*	Observed	Modeled	*R*	Observed	Modeled	*R*
CO, ppbv	172	196	0.91	146	177	0.60	110	119	0.37
O_3, ppbv	51.8	71.6	0.81	61.8	67.8	0.71	50. 2	54.3	0.54
Ethane, ppbv	1.86	1.90	0.82	1.43	1.41	0.16	0.93	0.73	0.27
Propane, ppbv	0.89	0.54	0.83	0.51	0.35	0.27	0.21	0.09	0.26
Ethyne, ppbv	0.45	0.41	0.87	0.28	0.27	0.46	0.18	0.09	0.22
SO_2, ppbv	1.16	0.40	0.48	0.70	0.64	0.31	0.26	0.16	−0.02
Acetone, ppbv	1.42	0.91	0.89	1.53	0.73	0.56	0.99	0.34	0.35
PAN, ppbv	0.23	0.96	0.60	0.79	0.85	−0.10	0.12	0.25	0.40
NO_2, ppbv	2.65	1.90	0.88	1.15	1.01	0.61	0.17	0.10	0.34
NO, ppbv	0.89	0.57	0.82	0.31	0.27	0.65	0.06	0.04	0.35
HNO_3, ppbv	1.39	1.17	0.86	1.58	1.28	0.68	0.33	0.36	0.73
NO_y, ppbv	5.45	6.78	0.92	3.38	4.98	0.61	0.78	1.11	0.47
NO_z, ppbv	2.40	4.31	0.95	2.13	3.69	0.60	0.61	0.98	0.56
Toluene, ppbv	0.156	0.174	0.91	0.069	0.109	0.67	0.029	0.017	0.25
Xylene, ppbv	0.165	0.091	0.84	0.034	0.039	0.72	0.004	0.003	0.26
$J[NO_2]$, 1/s	6.53×10^{-3}	6.90×10^{-3}	0.93	8.11×10^{-3}	7.86×10^{-3}	0.44	0.0084	0.0050	0.65
$J[O_3 \rightarrow O_2 + O^1D]$, 1/s	2.11×10^{-5}	2.07×10^{-5}	0.98	2.78×10^{-5}	2.29×10^{-5}	0.92	3.22×10^{-5}	1.38×10^{-5}	0.96
$J[H_2O_2]$, 1/s	4.31×10^{-6}	5.21×10^{-6}	0.97	5.61×10^{-6}	5.99×10^{-6}	0.68	6.08×10^{-6}	3.71×10^{-6}	0.89
$J[HNO_3]$, 1/s	3.77×10^{-7}	4.47×10^{-7}	0.98	4.96×10^{-7}	5.08×10^{-7}	0.84	5.53×10^{-7}	3.05×10^{-7}	0.94
$J[HNO_2 \rightarrow OH + NO]$, 1/s	1.43×10^{-3}	1.34×10^{-3}	0.94	1.79×10^{-3}	1.53×10^{-3}	0.46	1.88×10^{-3}	0.98×10^{-3}	0.68
$J[HCHO \rightarrow H + HCO]$, 1/s	1.86×10^{-5}	2.22×10^{-5}	0.98	2.45×10^{-5}	2.58×10^{-5}	0.72	2.76×10^{-5}	1.68×10^{-5}	0.90
$J[HCHO \rightarrow H_2 + CO]$, 1/s	3.11×10^{-5}	3.23×10^{-5}	0.96	4.13×10^{-5}	3.74×10^{-5}	0.58	4.57×10^{-5}	2.43×10^{-5}	0.79

>80% are presented in Tables 4 and 5, respectively. At altitudes below 1 km, the model performance for air masses with Asian ratio <20% was better than that with Asian ratio >80%, as represented by the *R* values for emitted short-lived species, such as SO_2, NO, NO_2, and their products HNO_3, NO_z, and NO_y. This decrease in performance with distance from the emission source areas is due to the accumulation of errors in the transport, chemistry and removal processes. This performance difference for emitted short-lived species also existed at the altitude 1–3 km, but not as significant as that below 1 km. At altitudes above 3 km, the model did not show any systematic differences between the high- and low-Asian-impact data sets.

[44] Further insights into the model performance are shown in Figure 12, where the observed and calculated CO distributions are presented. The observed CO distribution shows a high degree of variability with values of CO >160 ppbv found at all altitudes. The highest values, however, were found below 2 km around LA. The model shows the same basic behavior and is able to accurately capture the mean behavior (as shown in Table 3 where the model mean values are within 6% of the observations at all altitudes). The distribution of the bias (simulated-observed) is presented in Figure 12c. The estimated VOC age is shown in Figure 12d, and reveals that aged air is found at all attitudes and latitudes. No simple relationship appears

Table 5. Observed and Simulated (60-km Resolution) Mean Values and Their Correlation Coefficients *R* for ITCT 2K2: WP-3 Flights With CO Asian Ratio >80%

	Below 1 km			1 km to 3 km			Above 3 km		
Species and Variables	Observed	Modeled	*R*	Observed	Modeled	*R*	Observed	Modeled	*R*
CO, ppbv	129	121	0.90	127	118	0.46	125	112	0.085
O_3, ppbv	40.7	38.1	0.74	53.2	47.5	0.31	64.4	66.9	0.46
Ethane, ppbv	1.29	0.97	0.95	1.23	0.86	0.73	1.03	0.77	0.44
Propane, ppbv	0.20	0.11	0.97	0.18	0.08	0.87	0.13	0.06	0.33
Ethyne, ppbv	0.20	0.23	0.85	0.19	0.17	0.64	0.17	0.11	0.17
SO_2, ppbv	0.21	0.021	−0.02	0.21	0.09	0.35	0.32	0.11	0.26
Acetone, ppbv	0.48	0.43	0.77	0.86	0.35	−0.18	0.92	0.25	0.18
PAN, ppbv	0.060	0.075	0.77	0.089	0.094	0.76	0.15	0.14	0.33
NO_2, ppbv	0.25	0.020	0.12	0.035	0.011	−0.01	0.026	0.006	0.30
NO, ppbv	0.074	0.008	0.28	0.011	0.006	0.19	0.008	0.005	0.18
HNO_3, ppbv	0.077	0.058	−0.35	0.070	0.053	0.28	0.058	0.069	0.25
NO_y, ppbv	0.40	0.24	0.30	0.30	0.23	0.38	0.34	0.29	0.31
NO_z, ppbv	0.23	0.21	0.007	0.26	0.22	0.53	0.34	0.28	0.31
$J[NO_2]$, 1/s	7.53×10^{-3}	9.23×10^{-3}	0.31	9.88×10^{-3}	1.03×10^{-2}	0.61	0.0101	0.0104	0.63
$J[O_3 \rightarrow O_2 + O^1D]$, 1/s	1.89×10^{-5}	3.02×10^{-5}	0.72	3.23×10^{-5}	3.59×10^{-5}	0.81	2.88×10^{-5}	3.34×10^{-5}	0.83
$J[H_2O_2]$, 1/s	4.63×10^{-6}	7.13×10^{-6}	0.54	6.82×10^{-6}	8.30×10^{-6}	0.75	6.70×10^{-6}	8.22×10^{-6}	0.83
$J[HNO_3]$, 1/s	3.70×10^{-7}	6.26×10^{-7}	0.66	5.87×10^{-7}	7.33×10^{-7}	0.80	5.40×10^{-7}	6.94×10^{-7}	0.85
$J[HNO_2 \rightarrow OH + NO]$, 1/s	1.65×10^{-3}	1.80×10^{-3}	0.34	2.20×10^{-3}	2.02×10^{-3}	0.62	2.25×10^{-3}	2.06×10^{-3}	0.66
$J[HCHO \rightarrow H + HCO]$, 1/s	2.00×10^{-5}	3.16×10^{-5}	0.59	3.07×10^{-5}	3.78×10^{-5}	0.76	3.20×10^{-5}	3.94×10^{-5}	0.84
$J[HCHO \rightarrow H_2 + CO]$, 1/s	3.45×10^{-5}	4.45×10^{-5}	0.47	5.12×10^{-5}	5.21×10^{-5}	0.70	5.60×10^{-5}	5.42×10^{-5}	0.76

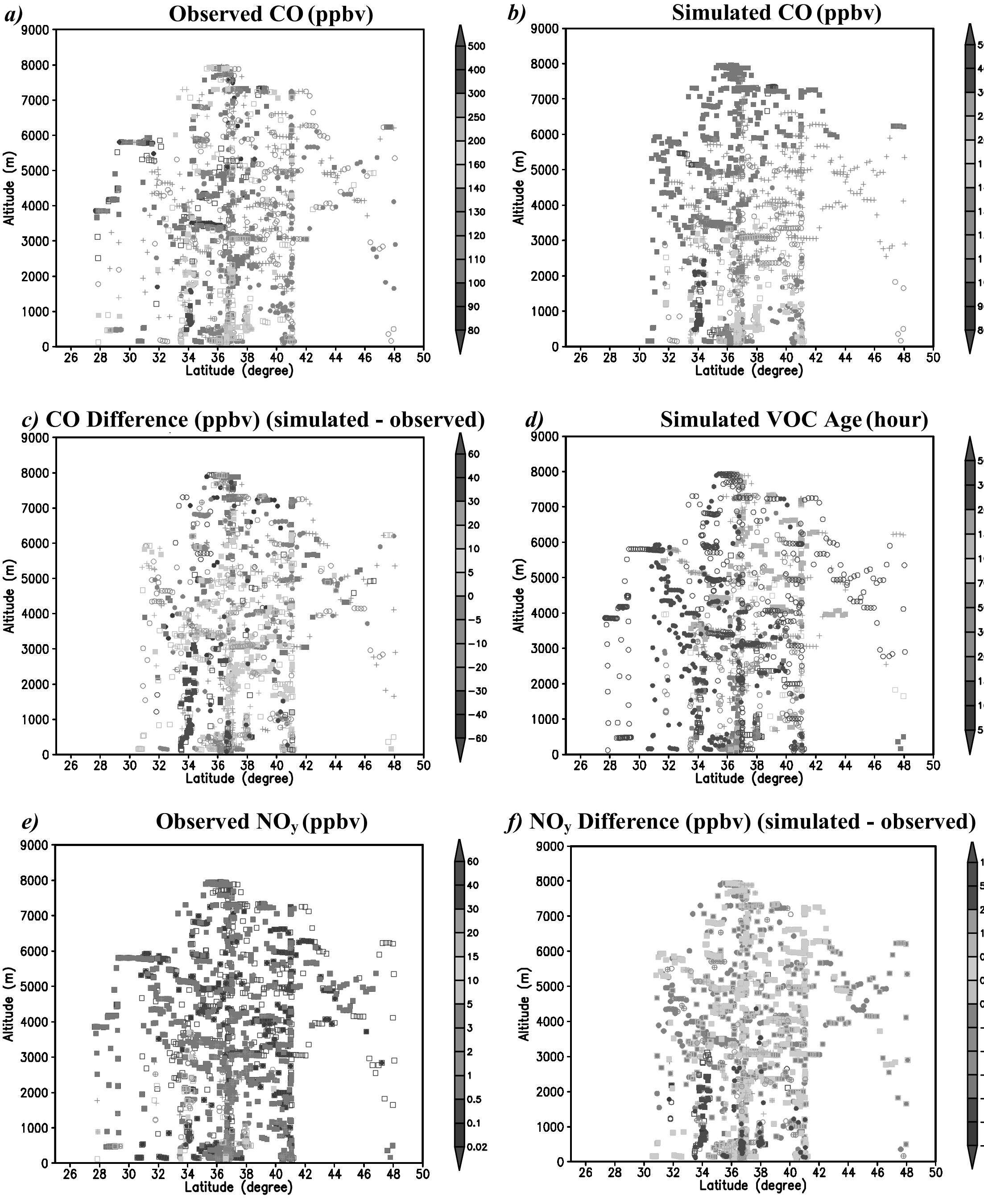

Figure 12. Latitude-altitude distributions of (a and b) CO, (c) CO difference, (d) VOC age, (e) NO_y, and (f) NO_y difference for all WP-3 flights. See color version of this figure at back of this issue.

between CO bias and air mass age. Similar results are found for observed and modeled NO_y.

8. Trinidad Head Surface Site

[45] During the ITCT 2K2 experiment extensive measurements were also performed at the Trinidad Head ground station (41.05°N, 124.15°W) located on the coast of northern California (Figure 1). The regional model was also used to provide forecast support and postanalysis interpretation to the surface observations. Figure 13 shows the model simulations compared to the surface measurements from Julian day 110 to 143 (10 April to 13 May). Figure 13a shows that simulated wind speeds agreed with the observed diurnal peak wind velocities, and reflected their daily variation trend. However, because of the relatively coarse resolution the RAMS prediction failed to represent the nighttime calm winds at Trinidad Head. Both the RAMS prediction and the observations showed that north and northeast winds prevailed (Figure 13b). The simulated CO and NO_y concentrations are consistent with the observation as shown in Figures 13c and 13d. Both the

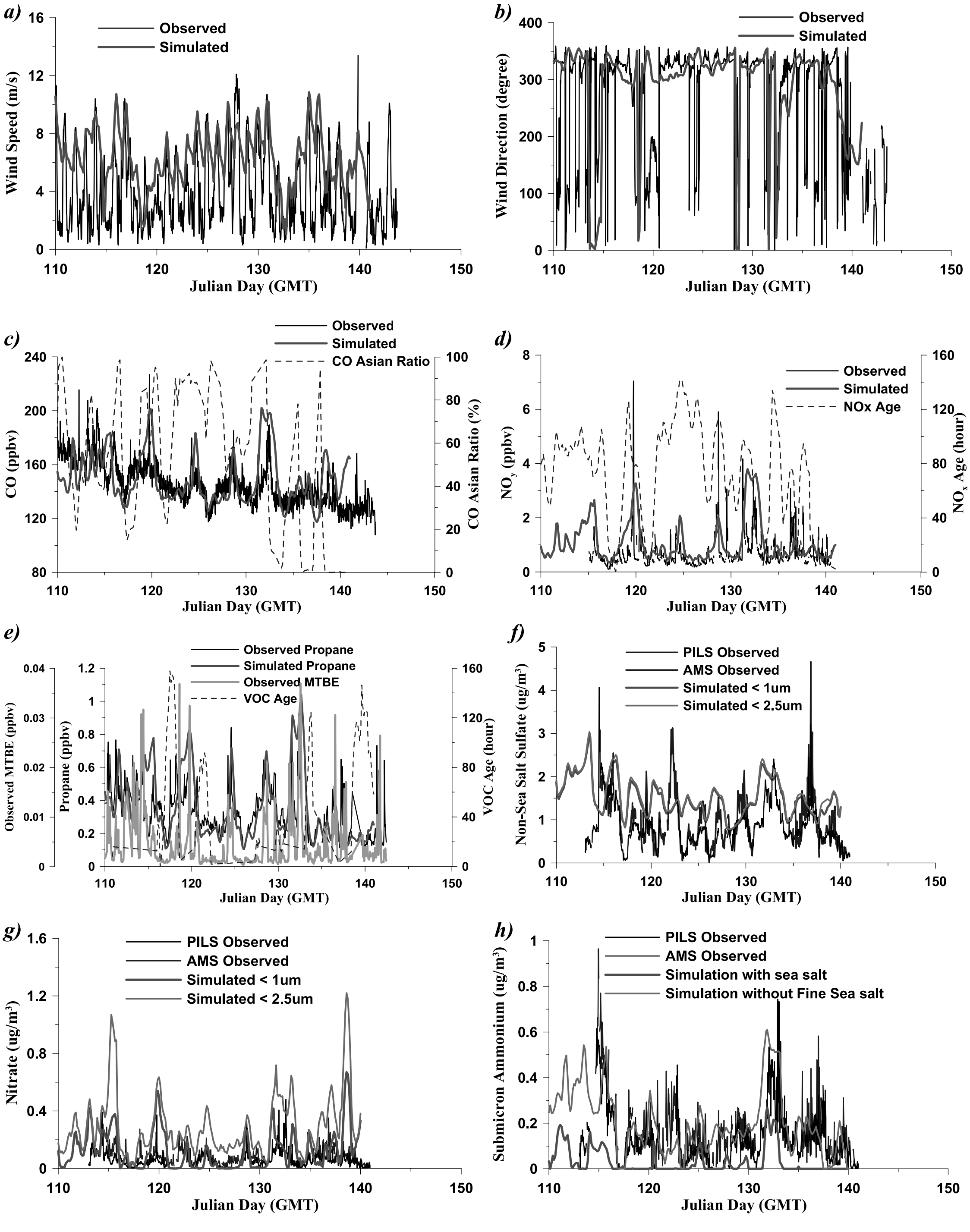

Figure 13. (a–h) Simulation compared to surface observations at Trinidad Head. See color version of this figure at back of this issue.

observed and the simulated values show that CO and NO_y are generally correlated. These two plots also show the CFORS simulated anthropogenic CO Asian ratio and NO_x age. In general CO Asian ratios >0.5 are associated with air masses older than 50 hours. The highest NO_y values occurred for air masses older than ~50 hours. For example the CO and NO_y peak concentrations on Julian days 113, 119–120, and 132 were associated with low surface wind speeds, implying that these peaks were mainly due to the accumulation of pollutants emitted from surrounding sources and transported to Trinidad Head under the low-wind-speed situations.

[46] Further insights into the role of local emission sources on Trinidad head is found in Figure 13e, where the simulated and observed propane, CFORS simulated VOC age, and observed methyl-t-butyl ether (MTBE), a compound mainly used in North America, are plotted. As shown the simulation results accurately capture the ob-

served propane features. MTBE is a good tracer for local sources, as shown by its plume-like structure [*Goldstein et al.*, 2004; *Millet et al.*, 2004]. The MTBE peaks correlate with peaks in propane (and other pollutants), but propane shows broader maxima, reflecting the longer lifetime of propane. The simulated VOC age shows clearly a reversed variation with observed MTBE, providing further evidence for the utility of the VOC age indicator in helping to identify local and distant sources. As shown by the CO results in Figure 13c, the fresh pollution events at Trinidad Head are superimposed on air that is a mixture of Asian and American sources.

[47] Both observed and simulated CO and propane show a clear declining trend during this one-month period (Figures 13c and 13e). The CO background concentration declined from 150 ppbv in April to 125 ppbv in May, while the propane background concentration declined from 0.3 to 0.15 ppbv. This seasonal variation trend reflects the increased CO and VOC consumptions by OH as the sunshine time became longer and photochemical reactions became more active (simulated daytime OH increased by about 30% during this period).

[48] There were two instruments measuring aerosol ions at Trinidad Head: particle-into-liquid sampler (PILS) and the aerodyne Aerosol Mass Spectrometer (AMS) [*Allan et al.*, 2004]. Both of these instruments report a cutoff diameter of ~1 μm to capture submicron ions. The measured and simulated aerosol sulfate, nitrate and ammonium concentrations are presented in Figures 13f, 13g, and 13h, respectively. As discussed by *Allan et al.* [2004], the AMS instrument observed consistently more nitrate than the PILS instrument. This may be due to the presence of organic nitrates and/or amines. The simulated nitrate values are shown in Figure 13g for <1-μm and <2.5-μm diameters. The model results show an appreciable amount of nitrate in particles with diameters between 1 μm and 2.5 μm. The simulation curves for <1 μm and <2.5 μm tend to encompass most of the observed nitrate, suggesting that differences in inlet cutoffs could account for some of the differences between the measurements. In fact, the AMS 1-μm cutoff diameter was not absolute, and the measurements included some particles between 1 and 2 μm. A second AMS instrument configured to study the more refractory aerosol fraction did identify submicron as well as supermicron nitrate, with the supermicron nitrate associated with sea-salt particles. The sea-salt mode is mainly in the supermicron regime, but the tail did go down into the submicron. The simulated fraction of nitrate in the supermicron particles varied from 5% to ~100%, with a mean value of 30%, and with the supermicron fraction dominating under elevated sea-salt conditions. Sea-salt nitrate was also linked to a suppression of chloride relative to sodium in the PILS observations as well as in the simulations.

[49] The simulated and observed ammonium values are shown in Figure 13h. The AMS and PILS measurements quantitatively agree (slope AMS versus PILS of 1.099, with r^2 of 0.58, *Allan et al.* [2004]). The model predictions are generally consistent with the observations, with essentially all of the ammonium in the particles below <1 μm, which was also verified by the AMS size-resolved measurements. Our prediction overestimated fine sea salt. After we removing this overestimation, ammonium prediction looks reasonable (Figure 13h).

9. Conclusion

[50] In this paper, a multiscale modeling system composed of a regional tracer model, a regional chemical transport model with a nested grid, and lateral boundary conditions from the global model MOZART was used to analyze aircraft and surface observations obtained during the ITCT 2K2 experiment. This model system was shown to have substantive predictive capability for the region and times of the NOAA WP-3 flights during the ITCT 2K2 experiment.

[51] The model estimated air mass source and chemical age indicators were used to help analyze the observations. The Asian air masses were found to have lower ΔAcetone/ΔCO, ΔMethanol/ΔCO, and ΔPropane/ΔEthyne ratios than air masses impacted by American sources. During the long-distance transport, Asian air masses experienced significant NO_y losses, associated with gas-aerosol interaction and removal processes. The VOC and NO_x age analysis indicated that air masses measured had chemical ages ranging from <0.5 to >10 days. Asian air masses were usually aged (>5 days). CO and O_3 were found to have net negative budgets in the places dominated by Asian influences, with CO losses due to reaction with OH, and O_3 lost via photolytic dissociation. In the MBL, OH levels were elevated and CO destruction was high. CO and O_3 chemical net budgets turned positive in polluted American air masses.

[52] The aerosol partitioning of nitrate was shown to be important. Without aerosol consideration, the model overestimated HNO_3, especially for its background concentration along the U.S West Coast. This result also implies that NO_y should decrease because of this process during the trans-Pacific transport.

[53] Several big cities exist along the U.S. West Coast. This study indicated that these cities received little Asian influence, and that photochemical processes were dominated by local sources. At Trinidad Head, most high concentrations of pollutants are associated with calm wind scenarios, and the accumulation of local sources. Seasonal variations of CO and VOCs showed a clear declining trend from April to May at this site. The high-resolution nested simulation greatly improved the prediction for emitted and secondary generated species. The resolution change affected not only the emission intensity and distribution, but also the associated photochemical behavior. In the coarse resolution (60-km) mode the concentrations of primary emitted species were underestimated, O_3 production was widespread, and the titrating effect of high-concentration pollutants was not resolved. This resulted in an overestimation of O_3, NO_z, and OH. The nesting simulation significantly improved the model performance.

[54] The multiscale modeling system consisting of nested models was shown to provide a viable tool for studying trans-Pacific transport, and the results were often consistent with observations. However, the difference between the simulations and measurements indicate that further improvements are needed to better quantify multiscale and multisource problems.

[55] **Acknowledgments.** This work was supported primarily by the NOAA Atmospheric Chemistry Program (grant NA16GP2315). Partial support was provided by the NSF Atmospheric Chemistry Program (NSF grant ATM-0002698), the NASA GTE and ACMAP programs, and the Department of Energy Atmospheric Chemistry Program. This work (I. Uno) was also partly supported by Research and Development Applying Advanced Computational Science and Technology (ACT-JST) and CREST of Japan Science and Technology Corporation. Special thanks go to Gerhard Hübler, Michael Trainer, and Fred Fehsenfeld for their efforts in the organization and execution of the ITCT 2K2 experiment. We also acknowledge the use of data collected by Joost de Gouw, J. Andy Neuman, David D. Parrish, Thomas B. Ryerson, Eric J. Williams, John B. Nowak, and their colleagues.

References

Allan, J. D., et al. (2004), Submicron aerosol composition at Trinidad Head, California, during ITCT 2K2: Its relationship with gas-phase volatile organic carbon and assessment of instrument performance, *J. Geophys. Res.*, *109*, D23S24, doi:10.1029/2003JD004208, in press.

Carmichael, G. R., et al. (2003a), Regional-scale chemical transport modeling in support of the analysis of observations obtained during the TRACE-P experiment, *J. Geophys. Res.*, *108*(D21), 8823, doi:10.1029/2002JD003117.

Carmichael, G. R., et al. (2003b), Evaluating regional emission estimates using the TRACE-P observations, *J. Geophys. Res.*, *108*(D21), 8810, doi:10.1029/2002JD003116.

Carter, W. (2000), Documentation of the SAPRC-99 chemical mechanism for voc reactivity assessment, final report to California Air Resources Board, contract 92–329, Univ. of Calif., Riverside,8 May .

Cooper, O. R., et al. (2004), A case study of transpacific warm conveyor belt transport: Influence of merging airstreams on trace gas import to North America, *J. Geophys. Res.*, *109*, D23S08, doi:10.1029/2003JD003624, in press.

Corbett, J. J., P. S. Fischbeck, and S. N. Pandis (1999), Global nitrogen and sulfur emissions inventories for oceangoing ships, *J. Geophys. Res.*, *104*(D3), 3457–3470.

de Gouw, J. A., et al. (2004), Chemical composition of air masses transported from Asia to the U.S. West Coast during ITCT 2K2: Fossil fuel combustion versus biomass-burning signatures, *J. Geophys. Res.*, *109*, D23S20, doi:10.1029/2003JD004202, in press.

Garratt, J. R. (1990), The internal boundary layer: A review, *Boundary Layer Meteorol.*, *50*, 171–203.

Goldstein, A. H., D. B. Millet, M. McKay, L. Jaeglé, L. Horowitz, O. Cooper, R. Hudman, D. J. Jacob, S. Oltmans, and A. Clarke (2004), Impact of Asian emissions on observations at Trinidad Head, California, during ITCT 2K2, *J. Geophys. Res.*, *109*, D23S17, doi:10.1029/2003JD004406, in press.

Guenther, A., et al. (1995), A global-model of natural volatile organic-compound emissions, *J. Geophys. Res.*, *100*(D5), 8873–8892.

Horowitz, L. W., et al. (2003), A global simulation of tropospheric ozone and related tracers: Description and evaluation of MOZART, version 2, *J. Geophys. Res.*, *108*(D24), 4784, doi:10.1029/2002JD002853.

Jacob, D. J., J. A. Logan, and P. P. Murti (1999), Effect of rising Asian emissions on surface ozone in the United States, *Geophys. Res. Lett.*, *26*, 2175–2178.

Jacob, D. J., J. H. Crawford, M. M. Kleb, V. S. Connors, R. J. Bendura, J. L. Raper, G. W. Sachse, J. C. Gille, L. Emmons, and C. L. Heald (2003), Transport and Chemical Evolution over the Pacific (TRACE-P) aircraft mission: Design, execution, and first results, *J. Geophys. Res.*, *108*(D20), 9000, doi:10.1029/2002JD003276.

Jaffe, D., et al. (1999), Transport of Asian air pollution to North America, *Geophys. Res. Lett.*, *26*, 711–714.

Jaffe, D., I. McKendry, T. Anderson, and H. Price (2003), Six 'new' episodes of trans-Pacific transport of air pollutants, *Atmos. Environ.*, *37*(3), 391–404.

Kim, Y. P., and J. H. Seinfeld (1995), Atmospheric gas-aerosol equilibrium. III: Thermodynamics of crustal elements Ca^{2+}, K^{+}, Mg^{2+}, *Aerosol Sci. Technol.*, *22*, 93–110.

Kim, Y. P., J. H. Seinfeld, and P. Saxena (1993a), Atmospheric gas-aerosol equilibrium. I: Thermodynamic model, *Aerosol Sci. Technol.*, *19*, 151–181.

Kim, Y. P., J. H. Seinfeld, and P. Saxena (1993b), Atmospheric gas-aerosol equilibrium. II: Analysis of common approximations and activity coefficient calculation methods, *Aerosol Sci. Technol.*, *19*, 182–198.

Kotchenruther, R. A., D. A. Jaffe, H. J. Beine, T. L. Anderson, J. W. Bottenheim, J. M. Harris, D. R. Blake, and R. Schmitt (2001), Observations of ozone and related species in the northeast Pacific during the PHOBEA campaigns: 2. Airborne observations, *J. Geophys. Res.*, *106*(D7), 7463–7483.

Kuhns, H., M. Green, and V. Etyemezian (2001), Big Bend Regional Aerosol and Visibility Observational (BRAVO) Study Modeling Emissions Inventory, report, Des. Res. Inst., Las Vegas, Nev.

Langmann, B., S. E. Bauer, and I. Bey (2003), The influence of the global photochemical composition of the troposphere on European summer smog, Part I: Application of a global to mesoscale model chain, *J. Geophys. Res.*, *108*(D4), 4146, doi:10.1029/2002JD002072.

Madronich, S., and S. Flocke (1999), The role of solar radiation in atmospheric chemistry, in *Handbook of Environmental Chemistry*, edited by P. Boule, pp. 1–26, Springer-Verlag, New York.

Millet, D. B., et al. (2004), Volatile organic compound measurements at Trinidad Head, California, during ITCT 2K2: Analysis of sources, atmospheric composition, and aerosol residence times, *J. Geophys. Res.*, *109*, D23S16, doi:10.1029/2003JD004026, in press.

Neuman, J. A., et al. (2003), Variability in ammonium nitrate formation and nitric acid depletion with altitude and location over California, *J. Geophys. Res.*, *108*(D17), 4557, doi:10.1029/2003JD003616.

Nowak, J. B., et al. (2004), Gas-phase chemical characteristics of Asian emission plumes observed during ITCT 2K2 over the eastern North Pacific Ocean, *J. Geophys. Res.*, *109*, D23S19, doi:10.1029/2003JD004488, in press.

Olivier, J. G. J., A. F. Bouwman, C. W. M. Van der Maas, J. J. M. Berdowski, J. P. J. Bloos, A. J. H. Visschedijk, P. Y. J. Zandveld, and J. L. Haverlag (1996), Description of EDGAR version 2.0: A set of global emission inventories of greenhouse gases and ozone-depleting substances for all anthropogenic and most natural sources on a per country basis and on 1° × 1° grid, *RIVM/TNO Rep. 771060002*, Natl. Inst. of Public Health and the Environ., Bilthoven, Netherlands.

Pickering, K. E., Y. S. Wang, W. K. Tao, C. Price, and J. F. Muller (1998), Vertical distributions of lightning NOx for use in regional and global chemical transport models, *J. Geophys. Res.*, *103*(D23), 31,203–31,216.

Pielke, R. A., et al. (1992), A comprehensive meteorological modeling system: RAMS, *Meteorol. Atmos. Phys.*, *49*, 69–91.

Strahan, S. E. (1999), Climatologies of lower stratospheric NO_y and O_3 and correlations with N_2O based on in situ observations, *J. Geophys. Res.*, *104*(D23), 30,463–30,480.

Streets, D. G., et al. (2003a), An inventory of gaseous and primary aerosol emissions in Asia in the year 2000, *J. Geophys. Res.*, *108*(D21), 8809, doi:10.1029/2002JD003093.

Streets, D. G., K. F. Yarber, J.-H. Woo, and G. R. Carmichael (2003b), Biomass burning in Asia: Annual and seasonal estimates and atmospheric emissions, *Global Biogeochem. Cycles*, *17*(4), 1099, doi:10.1029/2003GB002040.

Tang, Y. (2002), A case study of nesting simulation for the Southern Oxidants Study 1999 at Nashville, *Atmos. Environ.*, *36*(10), 1691–1705.

Tang, Y., et al. (2003a), Impacts of aerosols and clouds on photolysis frequencies and photochemistry during TRACE-P: 2. Three-dimensional study using a regional chemical transport model, *J. Geophys. Res.*, *108*(D21), 8822, doi:10.1029/2002JD003100.

Tang, Y., et al. (2003b), Influences of biomass burning during the Transport and Chemical Evolution Over the Pacific (TRACE-P) experiment identified by the regional chemical transport model, *J. Geophys. Res.*, *108*(D21), 8824, doi:10.1029/2002JD003110.

Tang, Y., et al. (2004), Three-dimensional simulations of inorganic aerosol distributions in east Asia during spring 2001, *J. Geophys. Res.*, *109*, doi:10.1029/2003JD004201, in press.

Trainer, M., et al. (1993), Correlation of ozone with NO_y in photochemical aged air, *J. Geophys. Res.*, *98*(D2), 2917–2925.

Uno, I. (2003), Regional chemical weather forecasting system CFORS: Model descriptions and analysis of surface observations at Japanese island stations during the ACE-Asia experiment, , *108*(D23), 8668, doi:10.1029/2002JD002845.

Uno, I., H. Amano, S. Emori, K. Kinoshita, I. Matsui, and N. Sugimoto (2001), Trans-Pacific yellow sand transport observed in April 1998: A numerical simulation, *J. Geophys. Res.*, *106*(D16), 18,331–18,344.

VanCuren, R. A., and T. A. Cahill (2002), Asian aerosols in North America: Frequency and concentration of fine dust, *J. Geophys. Res.*, *107*(D24), 4804, doi:10.1029/2002JD002204.

Woo, J.-H., et al. (2003), Contribution of biomass and biofuel emissions to trace gas distributions in Asia during the TRACE-P experiment, *J. Geophys. Res.*, *108*(D21), 8812, doi:10.1029/2002JD003200.

Yienger, J. J., M. Galanter, T. A. Holloway, M. J. Phadnis, S. K. Guttikunda, G. R. Carmichael, W. J. Moxim, and H. Levy (2000), The episodic nature of air pollution transport from Asia to North America, *J. Geophys. Res.*, *105*(D22), 26,931–26,945.

J. Allan, Department of Physics, University of Manchester Institute of Science and Technology, P. O. Box 88, Manchester M60 1QD, UK. (james.allan@physics.org)

E. C. Apel, E. Atlas, S. Donnelly, F. Flocke, K. Johnson, S. Schauffler, and V. Stroud, National Center for Atmospheric Research, 1850 Table Mesa

Drive, Boulder, CO 80307, USA. (apel@acd.ucar.edu; atlas@acd.ucar.edu; donnelly@ucar.edu; ffl@acd.ucar.edu; kristen.johnson@colorado.edu; sues@acd.ucar.edu; cstroud@acd.ucar.edu)

M. A. Avery, NASA Langley Research Center, Mail Stop 483, 21 Langley Boulevard, Hampton, VA 23681-2199, USA. (m.a.avery@larc.nasa.gov)

G. R. Carmichael, Y. Tang, and J.-H. Woo, Center for Global and Regional Environmental Research, University of Iowa, 402 IATL, Iowa City, IA 52242-1000, USA. (gcarmich@icaen.uiowa.edu; ytang@cgrer.uiowa.edu; woojh21@cgrer.uiowa.edu)

D. Dabdub, Department of Mechanical and Aerospace Engineering, University of California, Irvine, 4200 Engineering Gateway, Irvine, CA 92697-3975, USA. (ddabdub@uci.edu)

A. Goldstein and D. B. Millet, Department of Environmental Science, Policy, and Management, University of California, Berkeley, 151 Hilgard Hall, Berkeley, CA 94720-3110, USA. (ahg@nature.berkeley.edu;dylan@atmos.berkeley.edu)

L. W. Horowitz, Geophysical Fluid Dynamics Laboratory, NOAA, P.O. Box 308, Princeton, NJ 08542, USA. (larry.horowitz@noaa.gov)

L. G. Huey, School of Earth and Atmospheric Sciences, Georgia Institute of Technology, 221 Bobby Dodd Way, Atlanta, GA 30332-0340, USA. (greg.huey@eas.gatech.edu)

R. O. Jakoubek and J. M. Roberts, Aeronomy Laboratory, NOAA, 325 Broadway, Boulder, CO 80303, USA. (jakoubek@al.noaa.gov; jr@al.noaa.gov)

G. Kurata, Department of Ecological Engineering, Toyohashi University of Technology, Toyohashi, Aichi 441-8580, Japan. (kurata@eco.tut.ac.jp)

P. K. Quinn, Pacific Marine Environmental Laboratory, NOAA, 7600 Sand Point Way, NE, Seattle, WA 98115, USA. (quinn@pmel.noaa. gov)

A. Sandu, Department of Computer Science, Virginia Polytechnic Institute and State University, 660 McBryde Hall, Blacksburg, VA 24061, USA. (asandu@cs.vt.edu)

H. B. Singh, NASA Ames Research Center, Mail Stop 245-5, Moffett Field, CA 94035, USA. (hanwant.b.singh@nasa.gov)

D. G. Streets, Decision and Information Sciences Division, Argonne National Laboratory, DIS/900, 9700 South Cass Avenue, Argonne, IL 60439, USA. (dstreets@anl.gov)

I. Uno, Research Institute for Applied Mechanics, Kyushu University, 6-1 Kasuga-koen, Kasuga-shi, Fukuoka 816-8580, Japan. (iuno@riam.kyushu-u.ac.jp)

D. R. Worsnop, Center for Aerosol and Cloud Chemistry, Aerodyne Research Inc., 45 Manning Road, Billerica, MA 01821-3976, USA. (worsnop@aerodyne.com)

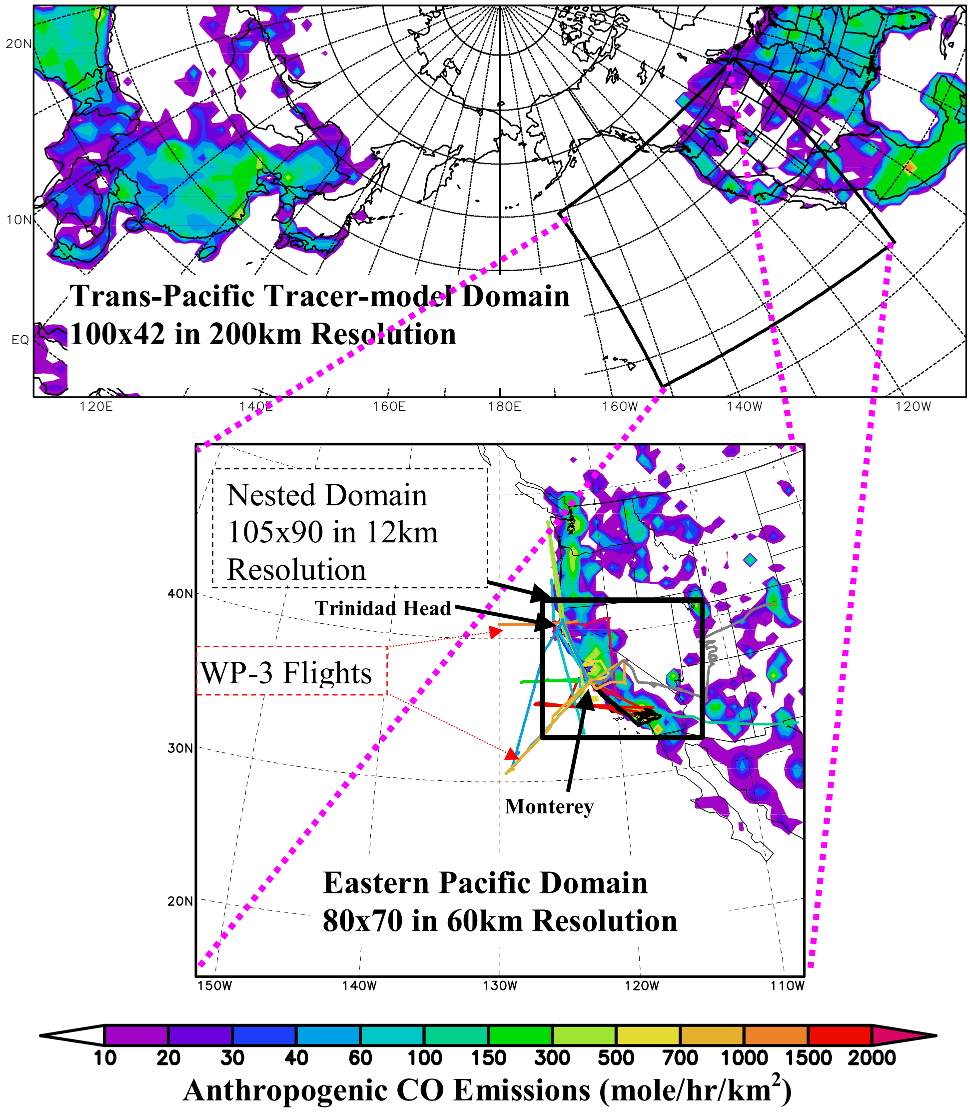

Figure 1. Model domains, NOAA WP-3 flight paths (colored lines), and estimated CO emissions on the various domains.

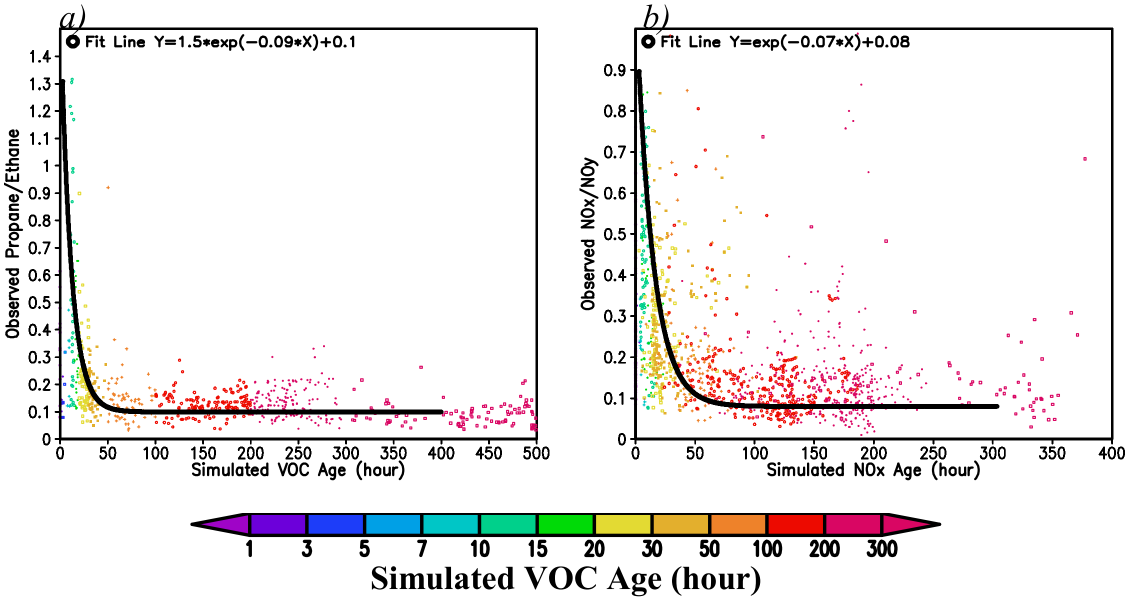

Figure 3. (a and b) Observed ratios versus VOC age and NO_x age estimated by the CFORS model for all ITCT flights, color-coded by VOC age.

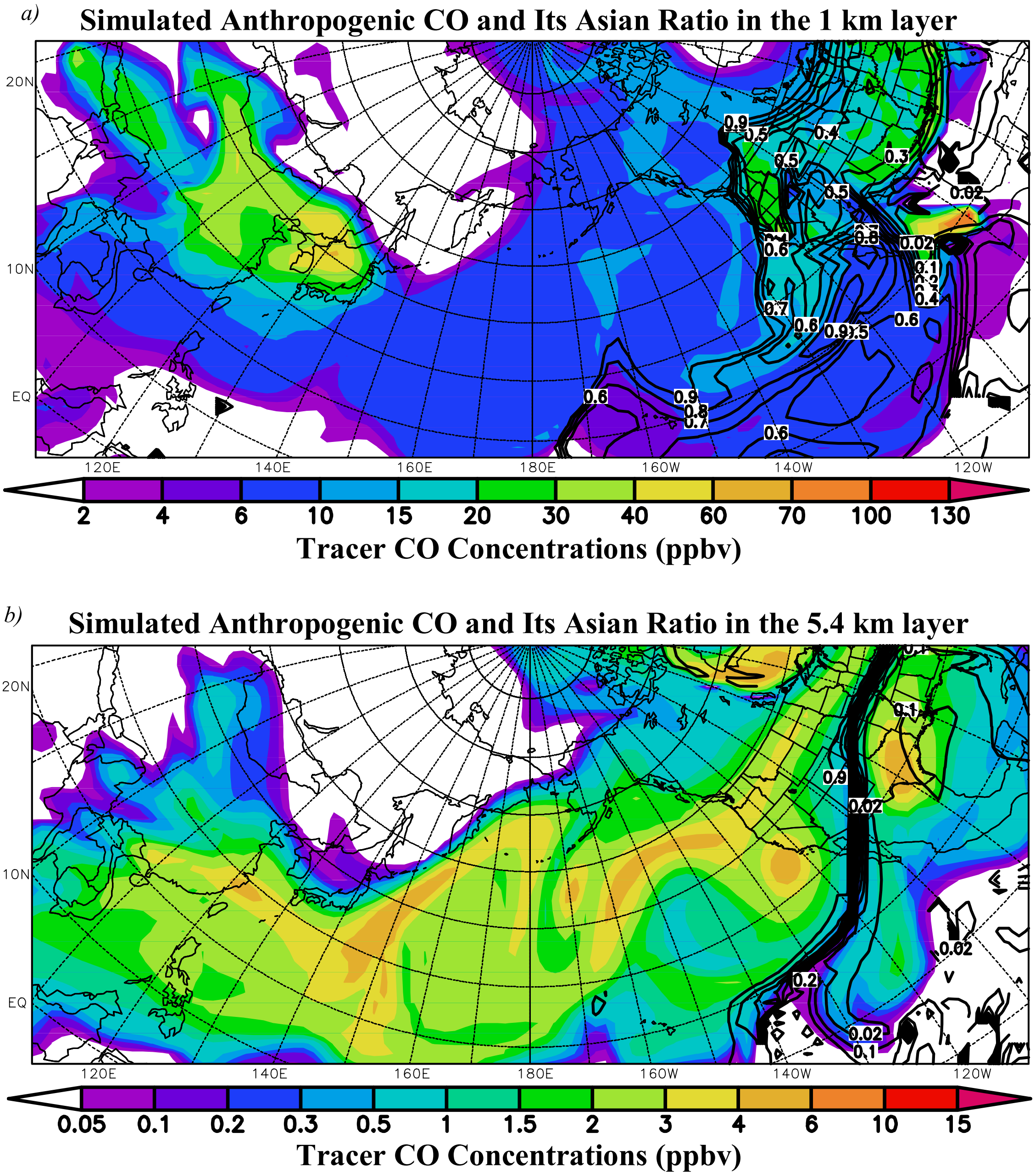

a) Simulated Anthropogenic CO and Its Asian Ratio in the 1 km layer

b) Simulated Anthropogenic CO and Its Asian Ratio in the 5.4 km layer

Figure 4. (a–f) Simulated results at 2100 GMT, 25 April 2002. CO Asian ratios are presented with contour lines in Figures 4a and 4b. CO and O_3 budgets are in ppbv/h.

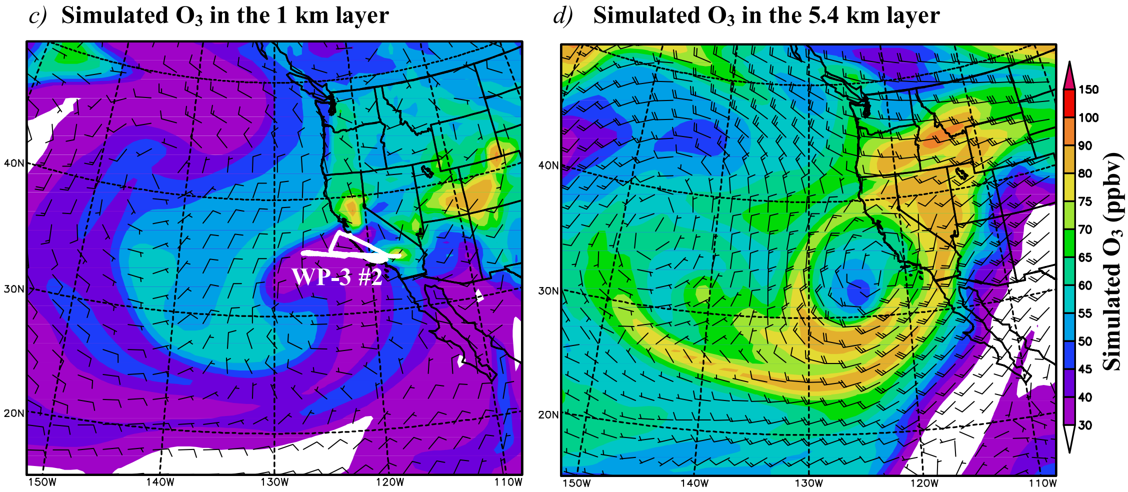

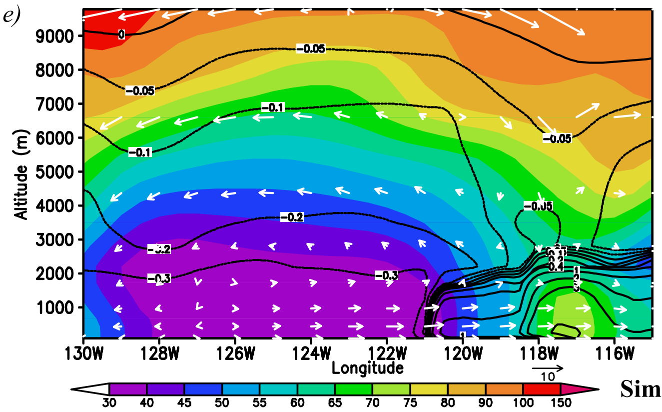

Simulated O_3 (color-coded) and its chemical net budget (contour) over latitude 35°N

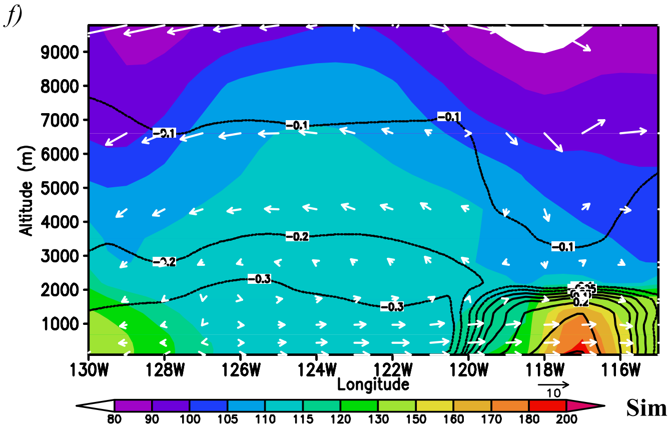

Simulated CO (color-coded) and its chemical net budget (contour) over latitude 35°N

Figure 4. (continued)

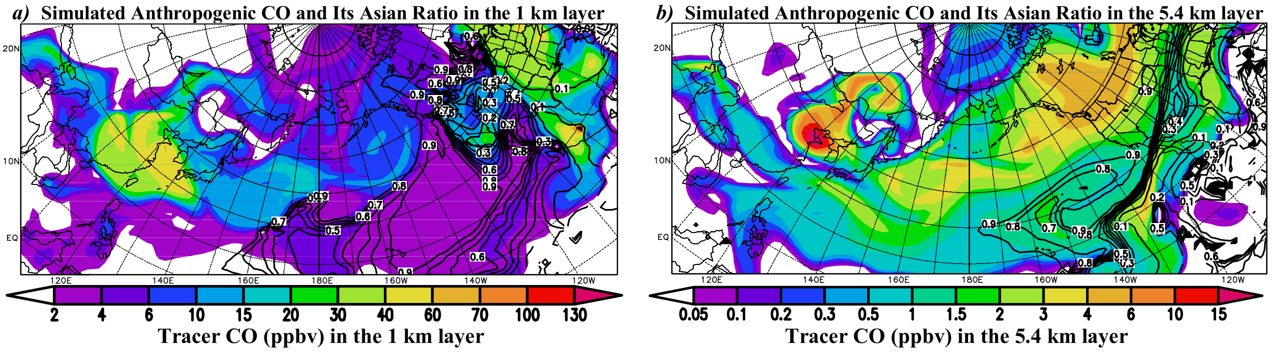
a) Simulated Anthropogenic CO and Its Asian Ratio in the 1 km layer

b) Simulated Anthropogenic CO and Its Asian Ratio in the 5.4 km layer

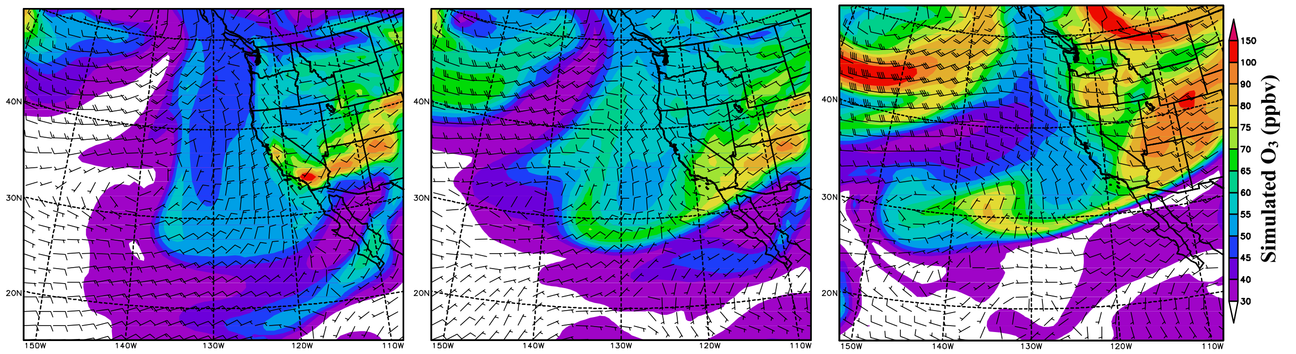
c) Simulated O_3 in the 1 km layer

d) Simulated O_3 in the 2.8 km layer

e) Simulated O_3 in the 5.4 km layer

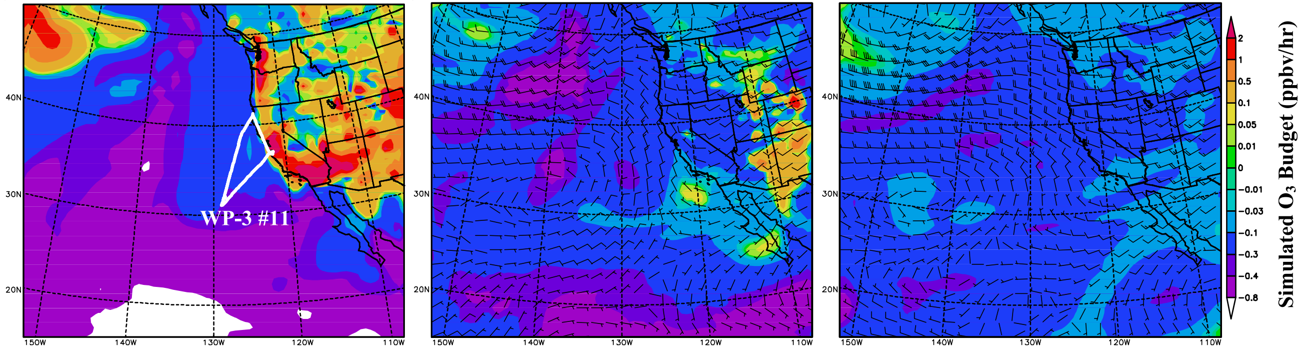
f) Simulated O_3 Budget in the 1 km layer

g) Simulated O_3 Budget in the 2.8 km layer

h) Simulated O_3 Budget in the 5.4 km layer

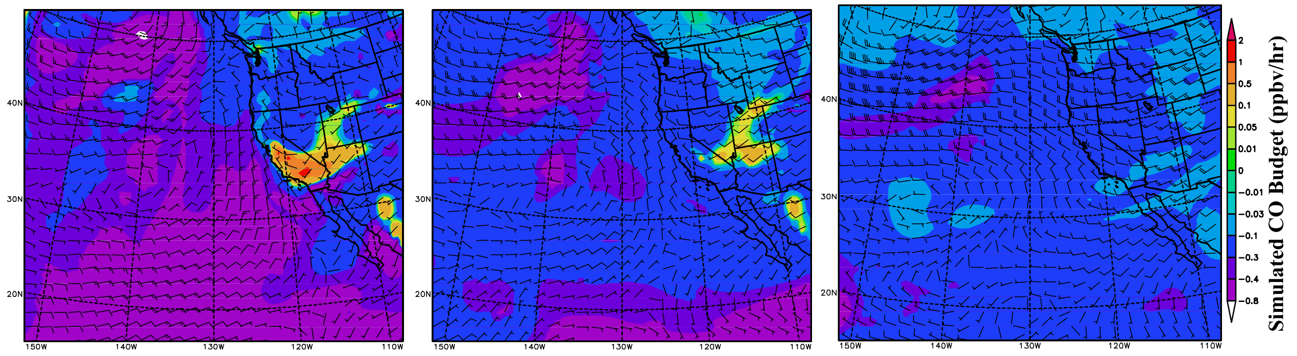
i) Simulated CO Budget in the 1 km layer

j) Simulated CO Budget in the 2.8 km layer

k) Simulated CO Budget in the 5.4 km layer

Figure 7. (a–k) Simulated results at 2100 GMT, 15 May 2002. CO Asian ratios are presented with contour lines in Figures 7a and 7b.

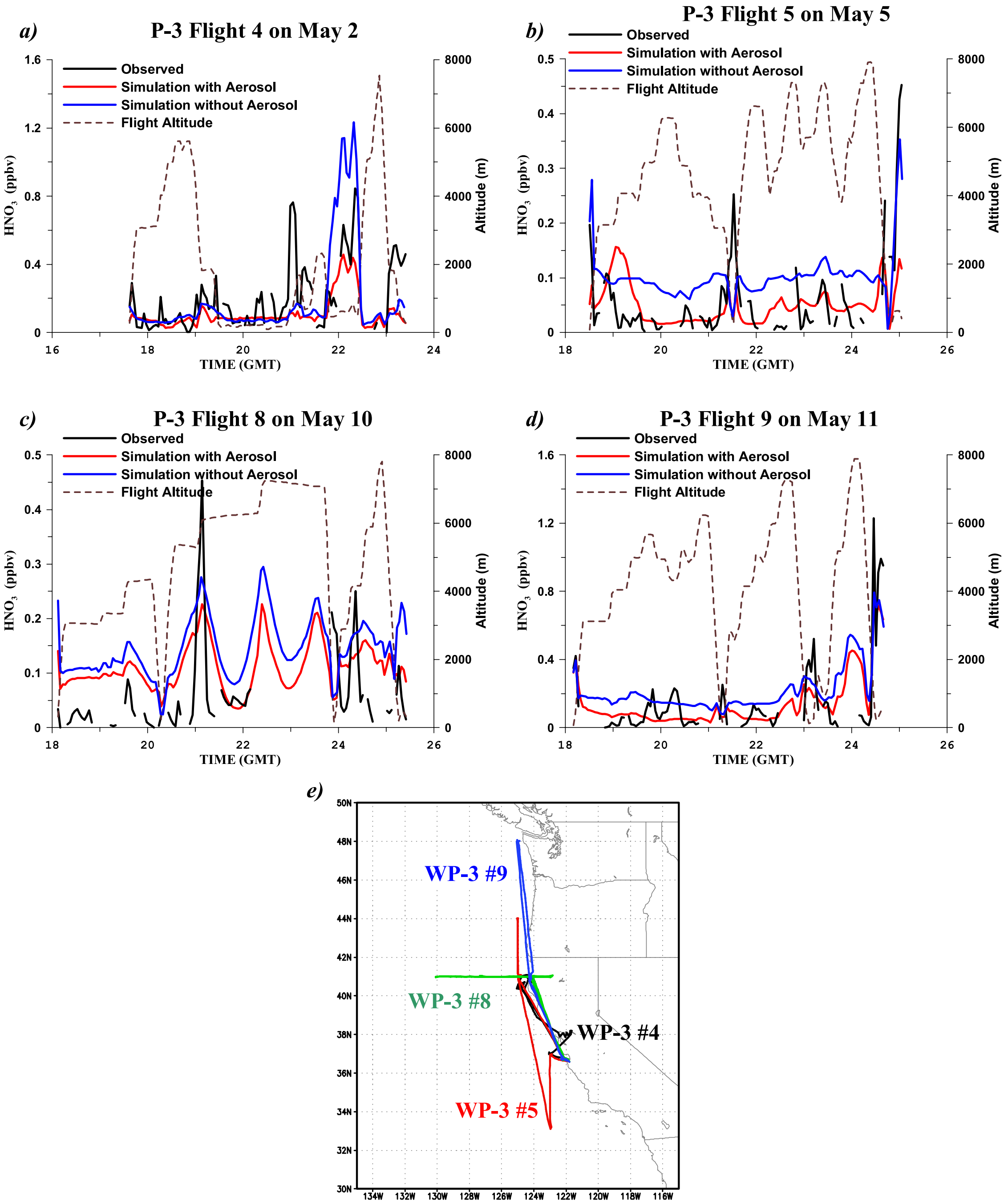

Figure 9. (a–e) STEM simulations with and without the aerosol consideration compared to observations of four WP-3 flights, whose paths are shown in Figure 9e.

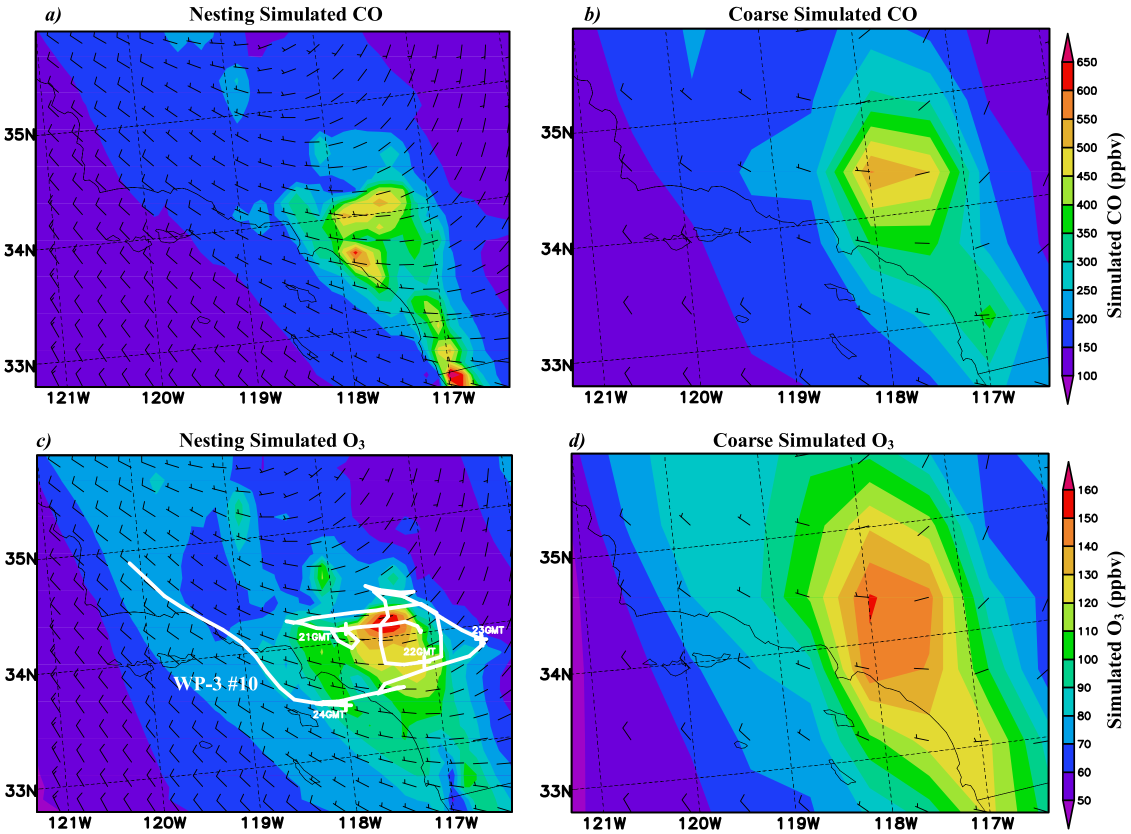

Figure 10. (a–d) Nested (12-km resolution) and coarse (60-km resolution) simulated CO and O_3 at 400 m at 2100 GMT, 13 May, for WP-3 flight 10 over Los Angeles and the surrounding area.

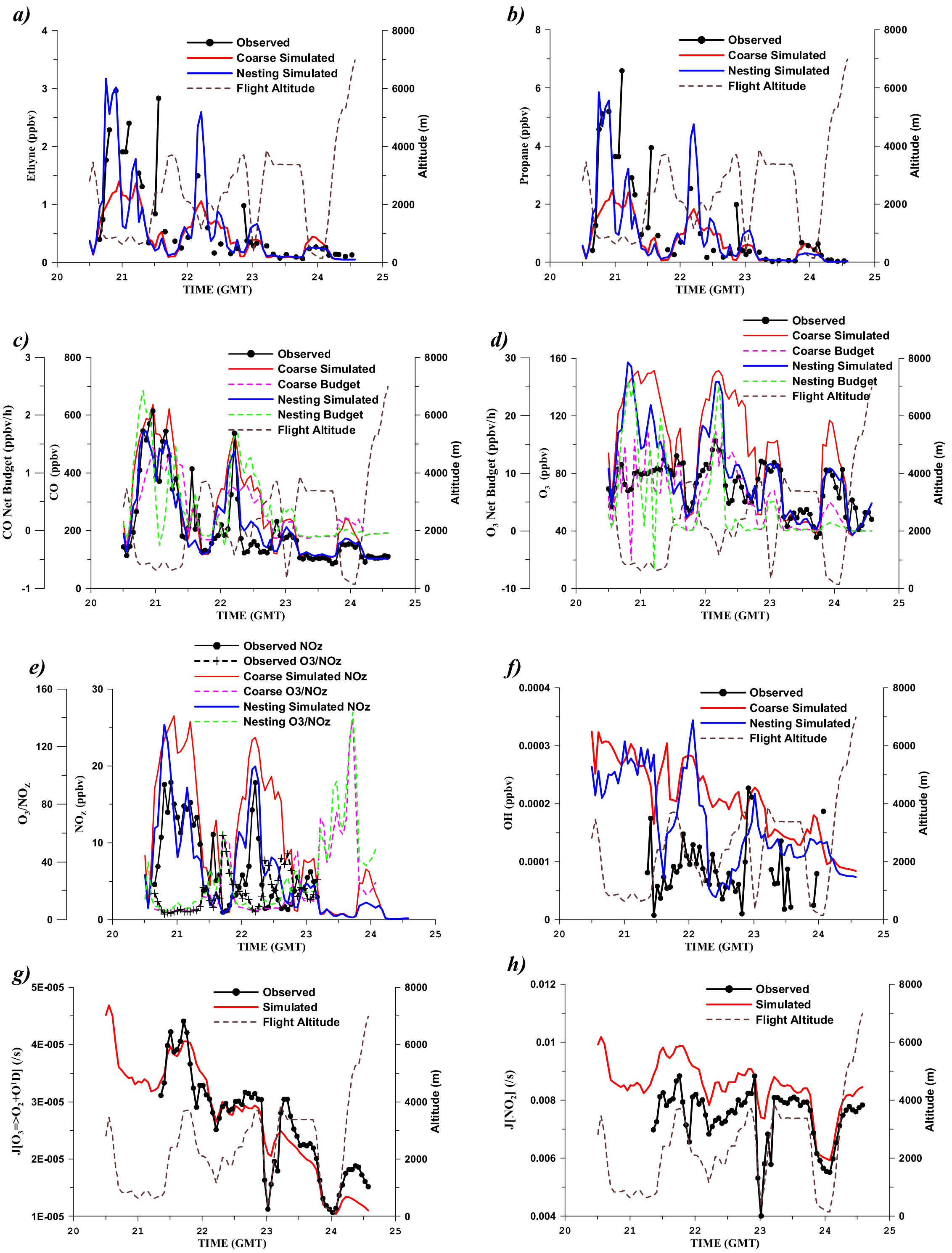

Figure 11. (a–h) Simulations compared to the measurements along the path of WP-3 flight 10 shown in Figure 10c. The nested and coarse simulations have similar *J* value predictions. So Figures 11g and 11h show only one simulation.

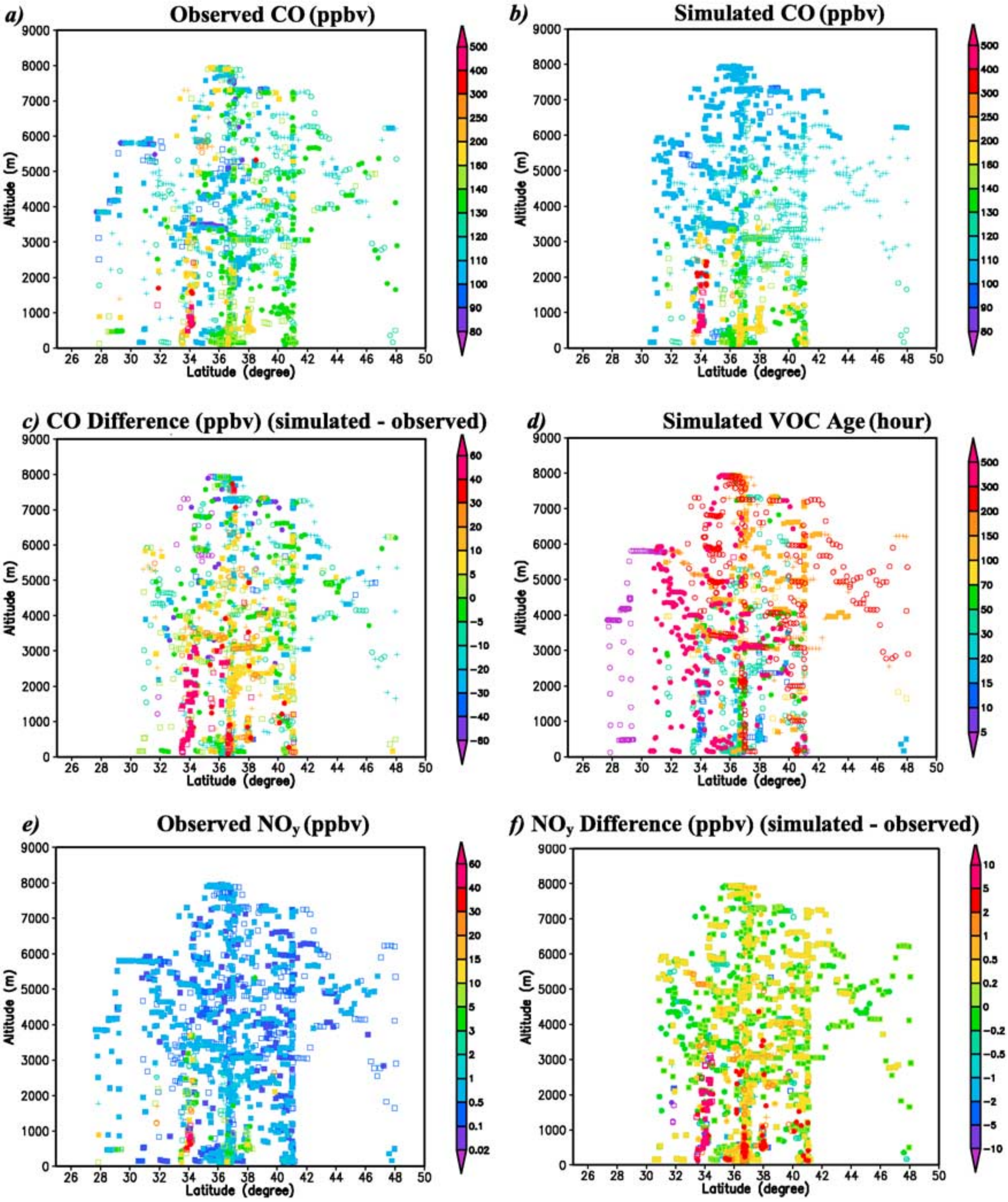

Figure 12. Latitude-altitude distributions of (a and b) CO, (c) CO difference, (d) VOC age, (e) NO_y, and (f) NO_y difference for all WP-3 flights.

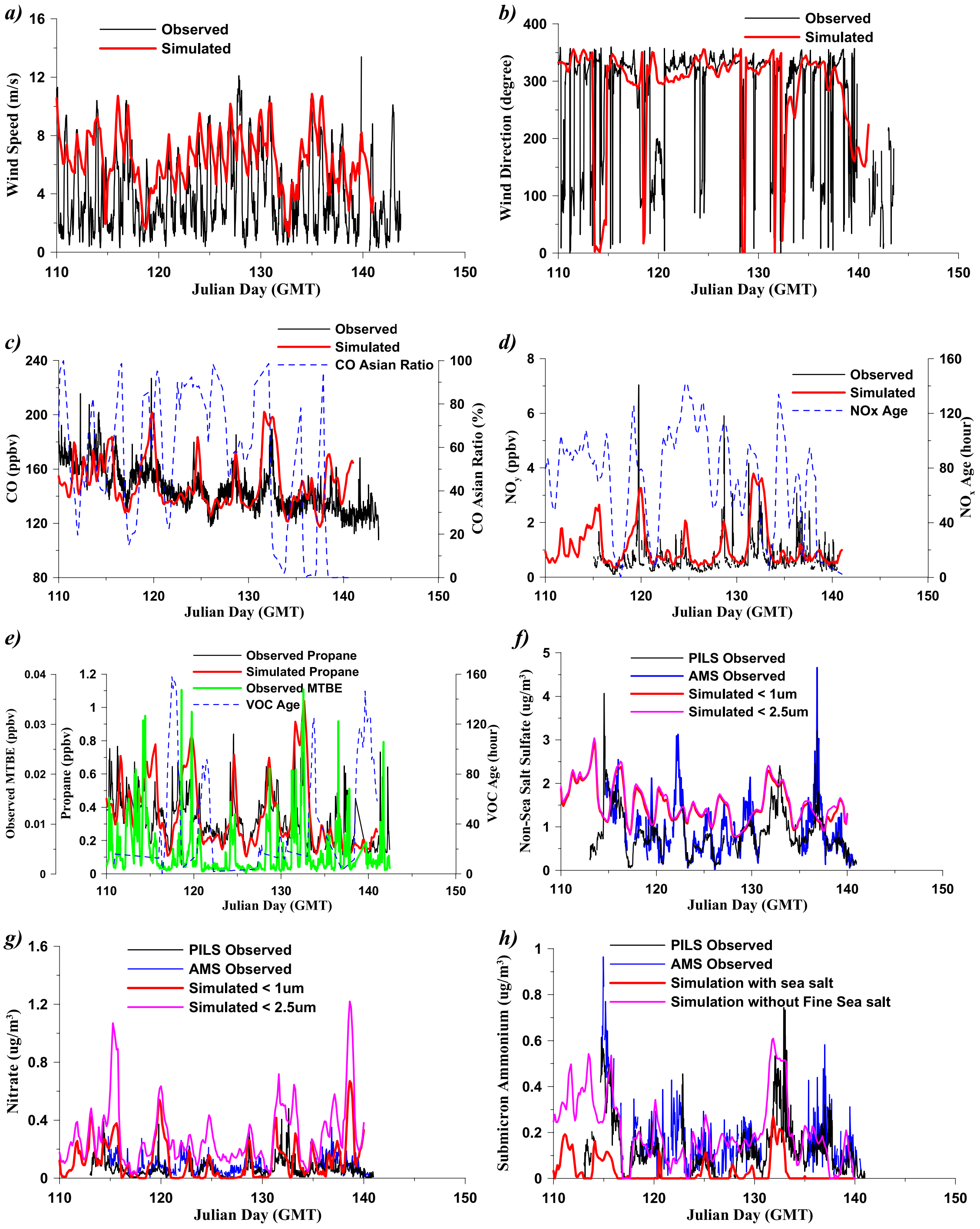

Figure 13. (a–h) Simulation compared to surface observations at Trinidad Head.